Energy 361 (2026) 141811

Contents lists available at ScienceDirect

Energy

journal homepage: www.elsevier.com/locate/energy

Parametric study of the techno-economic performance of Solar-MGT systems

Vahid Hosseini *, Noura Bettaieb, Tehmina Ambreen

School of Physics, Engineering and Computer Science, University of Hertfordshire, Hatfield, AL10 9AB, UK

ABSTRACT

Solar-assisted micro gas turbine (Solar-MGT) systems offer a promising solution for decentralised power generation by combining the reliability of gas turbines with the fuel-saving benefits of solar thermal input. This study presents a comprehensive techno-economic assessment of a Solar-MGT configuration using a detailed off-design model validated against both laboratory microturbine experiments and solar-assisted operation. A full-year simulation based on real meteorological data for Pretoria, South Africa captures the coupled effects of ambient conditions, receiver behaviour, Thermal Energy Storage (TES) operation, and component off-design performance within a unified framework. A refined component-level cost model is integrated into the analysis, enabling the influence of key subsystem characteristics on overall economic performance to be quantified.

An extensive parametric study evaluates the impact of turbine inlet temperature, dish area, TES mass and charging temperature, recuperator effectiveness, and system mass flow rate. When parameter variations are normalised to represent similar increases in capital expenditure, the resulting designs span fuel-to-electric efficiencies of about 14–30% and levelised costs of electricity in the range 0.4–0.8 €/kWh. Upgrades focused on turbomachinery efficiency or recuperator effectiveness deliver the lowest costs of electricity (down to ≈0.4–0.76 €/kWh), albeit with a modest reduction in solar share, whereas increases in dish area or operating temperature mainly raise the solar contribution with more limited economic benefit.

The findings demonstrate that optimal Solar-MGT performance arises from balanced combinations of design parameters rather than extreme values. The results highlight the importance of integrated, year-round techno-economic modelling for identifying realistic design pathways and guiding future Solar-MGT deployment.

Nomenclature

Symbol	Description
A	Area
C	Cost factor
CR_g	Geometrical concentration ratio
$C_{\min}$	Minimum heat capacity rate
$C_{\max}$	Maximum heat capacity rate
C_r	Ratio of heat capacity rates
E	Thermal energy
L	Length
Q	Thermal energy transfer
$\dot{Q}$	Thermal energy transfer rate
SC	Solar energy contribution in energy system
T	Temperature
W	Mechanical/electrical energy
$\dot{W}$	Mechanical/electrical energy rate
T	Temperature
U	Overall heat transfer coefficient
p	Pressure
h	Enthalpy
c_p	Specific heat at constant pressure
$\dot{m}$	Mass flow rate

(*continued on next column*)

(*continued*)

α	Absorptivity
ε	Effectiveness
η	Efficiency
σ	Stefan–Boltzmann constant
μ	Viscosity
ρ	Density
π	Pressure ratio
Subscripts	
0	Reference point
ambient	Ambient condition
in	Condition at inlet
C	Heat exchanger's cold path/Compressor
cc	Combustion chamber
d	Design point
h	Heat exchanger's hot path
in	Condition at inlet
out	Condition and exit
min	Minimum value
max	Maximum value
r	Ratio
ref	Reference point
T	Turbine

(*continued on next page*)

* Corresponding author.
E-mail address: v.hosseini@herts.ac.uk (V. Hosseini).

https://doi.org/10.1016/j.energy.2026.141811
Received 10 December 2025; Received in revised form 9 June 2026; Accepted 29 June 2026
Available online 30 July 2026

(*continued*)

Abbreviation	
BC	Boundary Condition
CAPEX	Capital Expenditure
DNI	Direct Normal Irradiation
DR	Discount Rate
EGT	Exhaust Gast Temperature
LCoE	Levelised Cost of Electricity
MGT	Micro Gas Turbine
NTU	Number of Transfer Units
O&M	Operation and Maintenance
SA	South Africa
SAURAN	Southern African Universities Radiometric Network
SC	Solar energy contribution in energy system
TES	Thermal Energy Storage
TIT	Turbine Inlet Temperature

1. Introduction

The increasing global energy demand, coupled with concerns over climate change and fossil fuel availability, particularly given that proven fossil fuel reserves correspond to only several decades of production at current rates [1], has intensified the focus on renewable energy systems. Among these, solar-based power generation has emerged as a promising solution for decentralised applications, where grid connectivity is either unreliable or economically unfeasible. In this context, interest in solar-thermal technologies has grown considerably in recent years [2], accompanied by rapid expansion in global Concentrated Solar Power (CSP) deployment [3]. Installed capacity reached about 6.7 GW in 2023, and projections indicate that CSP could supply around 11.3% of global electricity demand by 2050, with solar power forming a major share of this contribution [4]. However, the intermittent nature of solar energy presents a fundamental challenge in ensuring continuous and stable power supply [5], [6], [7], [8].

Hybrid energy systems that integrate renewable sources with conventional power generation technologies offer a viable approach to overcoming these limitations. Among dish-based CSP technologies, solar dish/Stirling systems have been widely investigated as an established point-focus configuration, particularly in terms of concentrator design, optical performance and system applications [9], [10]. Solar-assisted Micro Gas Turbine (Solar-MGT) systems have gained attention for their ability to combine solar-to-electric efficiency with the operational reliability of gas turbines. These systems leverage solar thermal energy to reduce fossil fuel consumption, thereby improving sustainability while maintaining a stable power output generation [11]. Additionally, incorporating Thermal Energy Storage (TES) into such systems enables excess solar thermal energy to be stored and dispatched during periods of low solar availability, reducing reliance on supplementary fossil fuel firing and enhancing operational flexibility [12], [13].

Despite their potential, Solar-MGT systems remain underexplored in terms of holistic performance analysis, particularly in real-world, off-design conditions. The interaction between solar energy availability, TES operation, and gas turbine efficiency introduces complex scenarios that require further investigation specifically in off-design conditions [11], [14]. Additionally, cost-effectiveness remains a major concern, as the economic viability of these systems depends on optimising capital and operational expenditures. A detailed techno-economic assessment is therefore essential to determine optimal design configurations that balance efficiency, reliability, and cost-effectiveness [13], [15], [16], [17], [18], [19].

Solar-assisted micro gas turbine (Solar-MGT) systems have been introduced as a promising solution for decentralised power generation. Research has demonstrated their potential for high efficiency, fuel savings, and hybrid operation flexibility [5], [6], [14], [20]. Two principal configurations exist: in pure-solar MGTs, the air receiver replaces the combustor [21]; in solar-assisted MGTs, the receiver preheats the compressed air upstream of the combustor, maintaining dispatchability with limited fuel use. European demonstration programmes such as SOLGATE (250 kWe) [22], SOLHYCO (100 kWe) [23] and SOLUGAS (4.6 MWe) [24] have verified the concept but also revealed enduring challenges, receiver durability, start-up control, and power-electronic limitations [25]. In a broader context, other initiatives such as the OMSOP (10 kWe) [26] investigated pure-solar MGT configurations without combustion chambers, and most recently POLYPHEM [27] explored solar-driven hybrid systems combining a micro gas turbine and a bottoming Organic Rankine Cycle with an integrated thermal storage device between the two cycles (40 kWe MGT + 20 kWe ORC).

Prior research on hybrid solar MGT systems has primarily emphasised solar components [28], [29], [30]. Relatively limited research attention has been directed toward gas turbine systems [24], [31], [32], [33]. Traditionally, the common strategy has been to utilise an existing micro gas turbine within the desired power range for integration with solar energy systems [33]. An alternative line of investigation has focused on developing solar micro gas turbine (MGT) systems using commercially available turbocharger components, as explored in several studies, [34], [19], [32], [33], and [25]. The use of turbocharger-based components offers a cost-effective and reliable solution for turbomachinery; however, such systems tend to experience reduced performance under off-design operating conditions.

Off-design, transient and optimisation-based frameworks have increasingly replaced simple design-point analyses in the modelling of solar-assisted Brayton systems over the past decade. OMSoP project was one of the first comprehensive efforts but mainly for pure solar MGT systems. Iaria and Nipkey [35] presented a thermodynamic–economic model for a 7 kWe pure solar MGT, validated against experimental data from Rome. Lanchi and Al-Zaili [36] extended the simulation to a quasi-steady annual estimation calibrated on the OMSoP prototype, integrating component maps and inverter limits; their results showed that neglecting generator constraints can bias output power estimates by more than ten percent. The component off-design effect was highlighted by Hampel et al. [37]. They reviewed the off-design modelling of the micro gas turbine systems and reported the lack of simulations in the available literature. They summarised that part-load studies are limited to Ansaldo AE-100 (formerly Turbec T100) and Capstone MGTs systems at ISO conditions (15 °C, 101.3 kPa, and 60% relative humidity), and if non-ISO conditions were considered, the works commonly did not consider or model part-load operation simultaneously. For pure solar MGT systems, Ghavami [38] advanced the field further through multi-objective optimisation of dish–MGT systems, demonstrating that dispatch strategy can influence the Levelised Cost of Energy (LCoE) as much as hardware improvements. They cited detailed off-design evaluations by Refs. [39], [40] which underlined the need to propagate component maps and pressure losses throughout the system model for similar pure solar arrangement. Similar off-design approaches applied by Refs. [36], [37] confirmed that simplified constant-efficiency assumptions tend to overpredict annual efficiency.

Thermal Energy Storage (TES) provides operational flexibility by decoupling solar input from power demand. Rodríguez-deArriba et al. [41] identified cost-effective designs that reduce total plant cost and levelised cost of electricity by 3.9% and 14.5% for different TES enabling cycle temperature at 550 °C and 700 °C, respectively, in a CO2-based Brayton cycle. Although based on a closed-cycle configuration, the study highlights the thermo-economic sensitivity of Brayton-type systems to TES temperature selection, a principle equally relevant to solar-assisted micro gas turbines. Fadzlin et al. [42] reviewed molten-salt, particle, and gas-based storage pathways for high-temperature CSP systems, identifying challenges of containment and corrosion beyond 700 °C. The time-dependent interaction between TES and Brayton-cycle systems has also been examined in sCO_2 configurations [43] and broader techno-economic assessments [44], reinforcing the need for annual, off-design simulations in evaluating hybrid solar-Brayton architectures. Though these targeted larger tower systems and lack the details of the power cycles off-design. Research has been widely conducted for the details of the TES component, mainly in large sizes [45], [46], [47], but few research on small scale systems (typically below ∼100 kW). For dish-based systems, compact latent-heat TES integrated with the air circuit has been studied to buffer thermal transients and maintain combustor inlet temperature [28]. For latent-heat TES concepts, the operating temperature is governed by the phase-change (melting) temperature of the storage material; empirical cost data summarised in Refs. [48] and [49] show that specific storage cost rises sharply with increasing melting temperature, constraining economic feasibility above about 750 °C. For solar-assisted MGT applications, both molten-salt tanks [50] and packed-bed [51] storage concepts have been investigated in the literature, with feasibility depending on operating temperature, scale, and integration constraints. Overall, TES enhances system dispatchability but introduces cost and pressure-drop penalties that must be evaluated through full-year off-design models. In the present study, a compact receiver-integrated latent-heat TES is adopted, consistent with solar-dish Brayton configurations [28], providing short-term thermal buffering and temperature stabilisation suitable for dish-scale Solar-MGT systems.

Peak Direct Normal Irradiance (DNI) typically occurs during the hottest hours of the day, when the micro gas turbine (MGT) operates at reduced efficiency due to elevated ambient temperatures. This mismatch underscores the need for high-resolution temporal modelling. Additional factors such as reciprocal shading between concentrators can further influence solar input and off-design operation. In solar-assisted micro gas turbine systems, however, the impact of shading on overall power output is mitigated by the ability to compensate reduced solar input with supplementary fuel firing. Hosseini et al. [52] showed that using hourly varying boundary conditions can alter annual fuel-consumption predictions by up to 7%, highlighting the importance of resolving short-term temperature and irradiance fluctuations. The requirement for temporal resolution becomes even more pronounced when a thermal energy storage (TES) unit is integrated into the loop, as storage charge–discharge depend strongly on transient solar and ambient conditions. Only a limited number of studies have performed annual analyses of solar–MGT systems while explicitly addressing off-design component behaviour. Existing work focuses mainly on solar-only configurations [36], [38], with a few examples in other solar-assisted systems ([2], [53], [54]). However, the literature has only partially explored how ambient temperature simultaneously affects MGT component performance and solar-receiver heat losses across the full operating range, and annual studies incorporating TES are still lacking.

Economic modelling of dish-based solar–MGT systems centres on three main components: solar field, MGT, and TES. The solar field and support structure constitute the dominant share of capital cost at small scale [15]. Detailed cost assessments by Gavagnin et al. [17] shows that the concentrator assembly, tracking mechanism, and installation logistics typically account for more than half of total system CAPEX. Their polynomial cost–area correlations capture the nonlinear growth in structural reinforcement and transport requirements as dish diameter increases. Second is the cost of MGT which there two approaches can be found in literature. The top-down approach which has been adopted by Refs. [17], [38] where the total micro gas turbine subsystem cost is expressed as a function of nominal capacity and technology level. These models are useful for system-level optimisation; however, they treat the MGT as a single aggregated cost block and therefore cannot resolve the influence of component-level performance metrics (e.g., compressor efficiency, recuperator effectiveness, pressure ratio) on subsystem CAPEX. As a result, valuable thermodynamic–economic interactions are lost, and the economic impact of component design choices cannot be quantified. The other approach, based on Massardo et al. works [55], [56], [57], [58], employs bottom-up cost functions for individual components (compressor, turbine, combustor, recuperator, generator) which has been widely adopted by many researchers [35], [59], [60], [61], [62]. These correlations explicitly link component cost to key design parameters and therefore enable a consistent thermodynamic–economic co-analysis. However, the original Massardo's coefficients were derived primarily for large industrial gas turbine and adapted for medium-scale MGTs, and when directly applied to modern small-scale under 100 kW (specifically under 10 kW), the model produces unrealistic component-level costs and distorted cost distributions. Weerakoon and Assadi [59], [60] report component costs for a 3 kW MGT of €16 (compressor), €106 (turbine), €57 (combustor), €53 (generator), and €4242 (recuperator), implying that the recuperator accounts for more than 90% of subsystem CAPEX. This distribution is inconsistent with aggregated cost breakdowns reported across small- and medium-scale MGT systems in recent review studies [63], [64], where the recuperator typically represents 26–30% of subsystem cost, and significant contributions arise from turbomachinery (14–25%), power conditioning and control (18–20%), and enclosure and balance-of-plant components (11–18%). While detailed, component-resolved TES cost modelling remains limited, empirical cost correlations such as [48] and [65] indicate that specific TES cost increases significantly with PCM melting temperature. This suggests that TES selection plays a non-negligible role in overall system economics, particularly in systems targeting high-temperature operation.

Although several studies have examined aspects of solar-assisted MGT systems, there is still no comprehensive annual analysis that simultaneously resolves component off-design behaviour, TES influence, and system-level techno-economic performance. Existing work typically isolates individual subsystems or evaluates short-term operation, leaving the combined impact of key design parameters under realistic, year-round conditions largely unexplored. A unified, experimentally validated framework is therefore needed to quantify how design choices shape both performance and cost in Solar-MGT systems. Table 1 summarises the modelling scope of representative Solar–MGT studies discussed above and highlights the remaining gap in annual, off-design, TES-integrated techno-economic assessment for solar-assisted configurations.

To address these gaps, this study aims to conduct a comprehensive parametric analysis of a Solar-MGT systems to investigate how key design parameters influence system performance and cost-effectiveness. Building on a detailed and experimentally validated off-design model, the work aims to quantify the effects of both MGT and solar system characteristics including Turbine Inlet Temperature (TIT), solar dish area, Thermal Energy Storage (TES) mass and temperature, and recuperator effectiveness. The focus is not merely on evaluating system performance but on developing a deeper understanding of how design trade-offs shape the overall techno-economic behaviour of Solar-MGT systems under real operating conditions.

Beyond combining sub-models, the contribution of this work lies in resolving (i) the coupled interactions between component off-design behaviour, (ii) TES transient operation, and (iii) techno-economic performance over a full year under realistic meteorological conditions, supported by an (iv) updated component-wise cost representation. This is essential because the same external drivers (irradiance and ambient temperature) simultaneously influence receiver thermal losses, turbine/compressor performance, and TES charge–discharge state, while economic outcomes depend on how design changes propagate to both fuel consumption and component-level capital cost.

To achieve this, a high-resolution annual simulation is performed using real meteorological data from Pretoria, South Africa, obtained from the publicly available SAURAN network [67], integrated with a techno-economic cost model, incorporating a component-wise cost representation. The simulation resolves hourly variations in ambient temperature and solar irradiance, enabling consistent representation of component off-design behaviour and TES charging–discharging dynamics throughout the year. Unlike previous studies that examined either technical or economic aspects in isolation, this work presents a unified framework that captures the complex interdependencies between thermal, solar, and economic subsystems. Moreover, the TES subsystem is treated as an active design variable, allowing assessment of

Table 1
Summary of representative Solar–MGT studies discussed in this paper and their modelling scope.

Study	System focus (as described)	Pure-solar/ Hybrid	TES integrated	Off-design with component maps	Ambient variability and part-load	Annual/ long-horizon simulation	Component level costing	Techno-economic metrics	Parametric, sensitivity analysis/ optimisation	Validation
[35]	7 kWe pure-solar MGT; thermo-economic model	pure solar	-	✓	✓	-	-	✓	-	✓
[25]	Quasi-steady off-design estimation of solar tower + MGT	hybrid	-	✓	✓	-	-	-	-	-
[36]	Quasi-steady annual estimation calibrated on OMSoP; includes inverter limits	pure solar	✓	✓	✓	✓	-	✓	-	limited
[38]	Dish–MGT pure-solar; multi-objective optimisation; dispatch matters for LCoE	pure solar	-	✓	✓	✓	-	✓	✓	limited
[52]	Hourly boundary conditions; annual fuel predictions sensitive to weather resolution	hybrid	-	✓	✓	✓	-	-	-	✓
[66]	Experimental testing of solar dish MGT with a downstream TES, steady-state simulation, validation	hybrid	✓	-	-	-	-	-	-	✓
[17]	Dish–MGT pure-solar; updated MGT, dish, and receiver costs as aggregated block	pure solar	-	✓	✓	✓	-	✓	✓	✓

its role in improving system flexibility, efficiency, and economic viability.

To the authors' knowledge, this research represents the first comprehensive parametric study of a Solar-MGT system conducted using a detailed, experimentally validated model. Previous studies, such as those by Refs. [25], [36], [38], have either analysed short-term performance, excluded TES, or neglected hybrid operation. In contrast, the present study combines a validated off-design performance model with full-year techno-economic evaluation, providing a more realistic and generalisable assessment of system behaviour. This integrated framework enables systematic evaluation of how key design parameters influence both annual thermodynamic performance and levelised cost of energy, thereby providing quantitative insight into performance–cost sensitivities under realistic year-round operation.

The paper is structured as follows; Section 2 presents a detailed description of the system configuration, the parametric study setup, and the modelling approach, including both the performance and techno-economic frameworks. Section 3 outlines the simulation assumptions and discusses the verification of both models. Section 4 presents the results of the parametric analysis, explores techno-economic trade-offs, and discusses model validation. Finally, Section 5 concludes the study with key findings and recommendations for future research and system design.

2. Methodology

The current study employs a comprehensive parametric and techno-economic analysis of a Solar-MGT system, integrating off-design performance modelling and cost evaluation. The methodology is structured to systematically investigate the impact of key design variables on system efficiency and financial viability under real-world meteorological conditions. Given the complexity of the system, verification is conducted separately for the performance and economic models to ensure consistency with experimental data and validated literature.

2.1. System description

The Solar-MGT system considered in this study consists of a solar concentrator (dish), a recuperated Micro Gas Turbine (MGT), and an integrated Thermal Energy Storage (TES) unit, as schematically illustrated in Fig. 1-a. The system is designed for hybrid operation, combining solar thermal input with supplementary fuel combustion (LPG in the present study). The solar dish concentrates direct normal irradiance onto a receiver, where compressed air upstream of the combustor is heated. The TES unit provides short-term thermal buffering, while the recuperator recovers turbine exhaust heat to enhance overall cycle efficiency. The illustrative T-s diagram and the principal thermodynamic states of the cycle are identified in Fig. 1-b. The corresponding design-point temperature, pressure, and mass flow rate, for an initial design of 3-5 kW system, are summarised in Table 2.

The MGT operates as a recuperated open Brayton cycle comprising a single-stage radial compressor and single-stage radial turbine, typical of small-scale microturbine architecture. Due to the relatively low-pressure ratio (below 5), turbine exhaust temperatures remain sufficiently high to justify heat recovery. The recuperator therefore preheats the compressed air prior to combustion, reducing fuel demand and improving cycle efficiency. Integration of solar heating and TES introduces an additional thermal input upstream of the combustor, enabling reduced fossil fuel consumption while maintaining dispatchable operation under varying solar and ambient conditions.

2.2. Parametric study setup

A structured parametric study is performed to assess the influence of key design parameters on system performance and economic viability. The one-at-a-time variation strategy adopted in this study is intentionally used to isolate the impact of individual design parameters and to enable a direct comparison of their relative influence on system performance and levelised cost. However, the proposed modelling framework is not limited to single-parameter interrogation as it resolves component off-design behaviour, receiver heat losses, TES

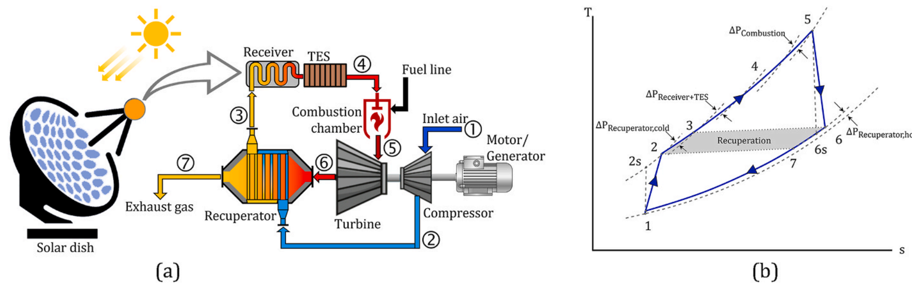

Fig. 1. Schematic arrangement of the integrated system of a parabolic solar dish and micro gas turbine equipped with thermal energy storage and recuperator.

Table 2
Design-point thermodynamic properties at the numbered stream locations shown in Fig. 1, evaluated under ISO ambient conditions.

Point	Location	Temperature [K]	Pressure [bar]
1	Compressor inlet	288.15	1.0132
2	Compressor outlet	438.39	3.0295
3	Recuperator cold-path outlet	886.35	2.9626
4	Receiver outlet	999.42	2.8441
5	Turbine inlet	1150.00	2.6559
6	Turbine exhaust	953.29	1.0412
7	Recuperator hot-path outlet	505.33	1.0133

charge–discharge dynamics, and techno-economic metrics within a single computational loop. The selected parameters and their significance are detailed as follows:

- Turbine Inlet Temperature (TIT): Increasing TIT improves thermal efficiency by enhancing the enthalpy drop across the turbine. However, higher TIT increases material stress, influencing component durability and maintenance costs. Variations in TIT naturally affect turbine exhaust temperature, which in turn influences recuperator inlet temperature and material requirements. Rather than constraining exhaust temperature, the present study allows this coupling to occur, and its economic implications are reflected within the recuperator cost model.
- MGT Mass Flow Rate: The design-point mass flow rate defines the nominal size of the micro gas turbine and directly influences power output, solar-to-fuel ratio, and capital cost. Variations in mass flow modify the thermal balance of the system and affect both economy and performance.
- Solar Dish Area: A larger dish increases solar input, reducing the need for fuel combustion at similar turbine inlet temperature settings. However, increasing dish size also raises capital costs, and the higher intercepted flux tends to increase receiver temperature and/or area, which in turn amplifies convective and radiative heat losses.
- TES Mass and Temperature: TES mass and operating temperature determine storage capacity and discharge capability under transient solar conditions, impacting the system's ability to maintain stable operation.
- Recuperator Effectiveness: Higher effectiveness improves heat recovery, reducing fuel consumption. However, increased heat exchanger surface area raises both pressure drop and investment cost, which are explicitly accounted for in the techno-economic model.

There are other Brayton-cycle variables, such as compressor pressure ratio, that influence the micro gas turbine and the overall system performance. In the present work, however, the compressor pressure ratio behaviour is intentionally kept similar to that of the reference design in order to preserve the underlying core-engine architecture, to focus the analysis on integration-level and thermal-balance-sensitive parameters.

The baseline values and bounds in Table 3 were selected to remain

Table 3
Base point and range of variation for parameters in the parametric study.

Parameter	Base Point Value	Range of Variation	Unit
TES Temperature	1000	950 - 1150	K
Turbine Inlet Temperature	1150	1050 -1250	K
Recuperator Effectiveness	0.9	0.75 - 0.95	-
Solar Dish Size	30	25 - 35	m^2
Mass Flow Rate	80	60 - 100	g/s
Electric power output	2.5	1.0 to 5.0	kW

within feasible dish-scale Solar-MGT design limits and to reflect typical ranges reported for micro gas turbines, recuperators, and receiver/TES integration in the Solar-MGT literature. Turbine inlet temperature and mass flow rate were limited by microturbine material and size considerations, while dish area and TES capacity were selected to represent realistic scales for decentralised and off-grid applications. The investigated ranges therefore span both conservative and advanced design options without departing from feasible system configurations.

2.3. Techno-economic model

The techno-economic model comprises two core components: the thermodynamic performance model and the cost model, both integrated to evaluate system efficiency and economic feasibility over an annual operational cycle.

2.3.1. Performance model

The thermodynamic performance of the Solar-MGT system is simulated using a component-based, off-design model developed in MATLAB. The modelling framework was introduced and validated in previous work [52] in steady-state condition, where both a recuperated MGT and a hybrid dish–MGT system were evaluated against experimental data. The present study builds on that validated framework and extends it to include a transient representation of the receiver-integrated TES operation.

The model considers.

- A 0-D energy balance is applied to each component (compressor, combustor, turbine, recuperator, receiver and TES).
- The air mass flow rate follows from compressor and turbine off-design maps combined with correlation-based pressure losses in the combustor, recuperator, receiver and ducts.
- Solar input at the receiver is computed from dish aperture, optical efficiency and DNI, while convective and radiative heat losses are explicitly included; radiative losses are evaluated owing to the high receiver temperatures.
- The TES is modelled by a lumped transient energy balance that tracks the internal energy of the phase change material, with charge and discharge driven by the temperature difference between the air and the TES.

- The recuperator is represented by its nominal effectiveness and pressure losses, and off-design outlet temperatures are obtained from an ε–NTU formulation.

Compressor and turbine performance are represented using off-design maps, so that flow rate, pressure ratio and efficiency are obtained consistently from corrected speed and corrected flow. This formulation allows variation of shaft rotational speed through compressor–turbine matching; however, in the parametric study presented in this paper the shaft speed is constrained to its design value in order to preserve the core-engine architecture and focus on integration-level parameters.

2.3.1.1. Governing equations. The transient performance of the Solar-MGT system was evaluated using a component-based energy model that applies the first law of thermodynamics to the system as a whole and to its subsystems. At every time step, the energy balance is constructed around the total rate of thermal input (from solar and fuel sources) and output (as net mechanical power and losses), while also tracking energy accumulation within the TES.

The 0-D governing equations of the components are presented in a generic form. A system-level matching algorithm is implemented to enforce mass and energy balance across the complete loop, including pressure losses in the combustor and recuperator, as well as thermal input from the receiver and TES. Gas turbine components and the overall matching algorithm are based on [68] but modified for each case which is explained in this section. The iterative solution ensures global consistency of mass flow rate, pressure ratio, and shaft work balance between compressor and turbine. The pressure and heat loss between the components are likewise modelled using a 0-D approach. The model is developed in MATLAB® [69]. The system of equations, including mass, energy, and heat transfer, is solved using a multi-dimensional Newton-Raphson method.

The energy conservation principle is expressed as:

$$\dot{Q}_{Solar} + \dot{Q}_{fuel} = \dot{W}_{net} + \dot{Q}_{loss} + \dot{Q}_{Storage} \qquad 1$$

The net mechanical output of the system is the difference between turbine and compressor work, corrected by generator and mechanical losses:

$$\dot{W}_{net} = \left(\dot{W}_{Turbine} - \dot{W}_{Compressor}\right) \cdot \eta_{mechanical} \cdot \eta_{Generator} \qquad 2$$

The work produced by the turbine and consumed by the compressor are obtained from enthalpy differences across each component assuming each of them as a single stage:

$$\dot{W}_{Compressor} = \dot{m}_{air}\left(h_{C,out} - h_{C,in}\right) \qquad 3$$

$$\dot{W}_{Turbine} = \dot{m}_{gas}\left(h_{T,in} - h_{T,out}\right) \qquad 4$$

The outlet temperature of the compressor and turbine can be calculated by the isentropic efficiencies:

$$T_{C,out} = T_{C,in}\left(1 + \left(\left(p_{C,out}/p_{C,in}\right)^{(\gamma-1)/\gamma} - 1\right) \Big/ \eta_{Compressor}\right) \qquad 5$$

$$T_{T,out} = T_{T,in}\left(1 - \eta_{Turbine}\left(1 - \left(P_{T,in}/P_{T,out}\right)^{(\gamma-1)/\gamma}\right)\right) \qquad 6$$

where the subscribes $_{C,in}$, $_{C,out}$, $_{T,in}$, and $_{T,out}$ refers to compressor inlet, compressor outlet, turbine inlet and turbine outlet, respectively. Compressor and turbine performance maps are generated using constant speed scaling of a reference map [52]. The scaling includes Reynolds number index correction to account for size-related efficiency variation [70]. The resulting maps are then used for off-design performance calculations.

At compressor, air is treated as a perfect gas with temperature-dependent specific heat capacity, using polynomial correlations reported by Ref. [68]. On the turbine side, the working fluid is modelled as a perfect gas mixture composed of the principal combustion species (N_2, O_2, CO_2, H_2O). The mixture specific heat is evaluated by mass-fraction-weighted averaging of species properties, each expressed as a temperature-dependent polynomial from Ref. [68].

The solar subsystem consists of a single parabolic dish directly coupled to the receiver. The solar energy that transfers to the working fluid $\dot{Q}_{Solar}$ is a function of the DNI, optical efficiency of the solar dish, and the collector area. The net heat transferred to the receiver fluid is corrected by the thermal losses from the receiver cavity, which includes both convective and radiative mechanisms:

$$\dot{Q}_{Solar} = \eta_{Solar} A_{Dish} DNI \qquad 7$$

$$\eta_{Solar} = \eta_{Dish}\alpha_{Receiver} - \frac{\sigma\varepsilon_{Receiver}\left(T_{Receiver}{}^{4} - T_{Sky}{}^{4}\right)}{CR_g DNI} - \frac{U\left(T_{Receiver} - T_{Ambient}\right)}{CR_g DNI} \qquad 8$$

where A_{dish}, η_{Dish}, $\alpha_{Receiver}$, $\varepsilon_{Receiver}$, and σ are the dish aperture area, dish reflection efficiency, absorptivity of the receiver, emissivity of the receiver, and the Stefan–Boltzmann constant, respectively, and η_{Solar} presents the overall solar efficiency. The effective sky temperature T_{sky} is assumed constant and equal to 275 K [38]. The geometric concentration ratio CR_g is defined as the ratio of the dish aperture area to the receiver aperture area, $CR_g = A_{dish}/A_{receiver}$.

The fuel energy input $\dot{Q}_{fuel}$ is derived from the internal energy deficit after solar and recuperative preheating, determined by the combustion chamber requirement to reach the prescribed TIT. The heat transferred from the recuperator is determined by its effectiveness (ε):

$$\dot{Q}_{recuperated} = \varepsilon_{Recuperator} \times \min\left(C_{cold}, C_{hot}\right) \times \left(T_{hot,in} - T_{cold,in}\right); \; C = \dot{m}c_p \qquad 9$$

This increases the pre-combustion air temperature, thereby reducing the required fuel input. The fuel mass flow rate is then computed as:

$$\dot{m}_{fuel} = \left(\dot{m}_{gas}h_{combustion,out} - \dot{m}_{air}h_{combustion,in}\right) \Big/ \left(LHV_{fuel} \cdot \eta_{combustion}\right) \qquad 10$$

where LHV_{fuel} is the lower heating value of the fuel and $\eta_{combustion}$ is the combustion efficiency.

The TES term $\dot{Q}_{Storage}$ can be evaluated using the energy balance for the storage considering the energy input from the solar system and the energy output by the working fluid (equation (11)).

$$\dot{Q}_{Storage} = \dot{Q}_{in} - \dot{Q}_{out} \qquad 11$$

The TES considered in this study is a receiver-integrated latent-heat storage based on solid–liquid phase change material (PCM). The storage is modelled as a lumped thermal mass, and its state is represented by the total internal energy E_{state} (Fig. 2). During charging, solar heat increases the PCM temperature to the melting point and subsequently drives the phase transition; during discharging, stored latent and sensible heat is transferred to the working fluid. The storage state is therefore

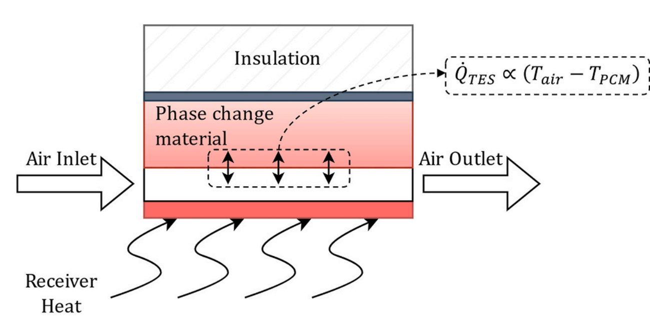

Fig. 2. Schematic arrangement of the integrated system of a parabolic solar dish and micro gas turbine equipped with thermal energy storage and recuperator.

characterised by the liquid fraction of the PCM, which is determined from the stored energy level. Spatial temperature gradients and phase-front dynamics are not explicitly resolved.

The amount of stored energy in TES, ${E_{state}}^n$, is dependent on its charging state (the amount of energy that has already been stored, ${E_{state}}^{n-1}$) which can be characterised by the amount of liquified material. The energy balance and the state of the energy storage is sequentially calculated by equation (12):

$$ {E_{state}}^n = {E_{state}}^{n-1} + Q_{in} - Q_{out} \tag{12} $$

where Q represents the time-integrated heat transfer over the time step, calculated from the heat transfer rate ($\dot{Q}$) as $Q = \dot{Q}\Delta t$, and n represents the discrete simulation time-step, and Δt is the fixed temporal resolution of the annual simulation.

The energy losses account for all other energy escaping the system boundary, including piping losses, and inefficiencies in the recuperator and TES insulation. These losses increase with larger temperature differences between hot components and the ambient environment. Thermal losses from the receiver cavity are explicitly modelled through radiative and convective heat transfer. Heat losses from the TES are represented using a lumped round-trip efficiency assumption corresponding to 10% of the stored energy per 24-h period. Details of pressure loss calculations in each component are based on the calculations from Ref. [52].

2.3.1.2. Performance indicators. To evaluate the technical performance of the system, three primary indicators are used in this study. The *fuel-to-electric efficiency* is defined as the ratio of net electric power output to the energy input from the fuel, equation (13):

$$ \eta_{fuel-power} = \frac{\dot{W}_{net}}{\dot{Q}_{in,fuel}} \tag{13} $$

The *solar fraction* (*solar share*) represents the contribution of solar energy to the total thermal input and is defined as equation (14):

$$ SC = \frac{\dot{Q}_{in,Solar}}{\dot{Q}_{in,Solar} + \dot{Q}_{in,fuel}} \tag{14} $$

The overall thermal efficiency of the hybrid system is defined as the ratio of net electric output to the total thermal energy input from both fuel and solar sources, equation (15):

$$ \eta_{thermal-power} = \frac{\dot{W}_{net}}{\dot{Q}_{in,fuel} + \dot{Q}_{in,Solar}} \tag{15} $$

where $\dot{W}_{net}$, $\dot{Q}_{in,fuel}$, and $\dot{Q}_{in,Solar}$ are the electrical power output, energy content of the consumed fuel, and incident solar heat on the solar dish, respectively. For annual performance assessment, these quantities are evaluated on a time-integrated basis over the simulation period.

2.3.2. Cost model

The techno-economic behaviour of the Solar-MGT system is assessed using a component-based cost model coupled to the annual performance simulation. Economic viability is quantified in terms of the Levelised Cost of Electricity (LCoE), which reflects the discounted cost of capital expenditure, fuel consumption, and Operation and Maintenance (O&M), relative to the net electrical output of the plant, thereby linking economic viability directly to the performance outputs [18], [38], [71]. The present work utilised the component-wise cost functions of the MGT presented in Ref. [55] and update it using available literature [17], [71], [72] to evaluate system cost through analytical functions derived from components' design characteristics.

At each parametric configuration, the total annual cost of electricity generation is obtained as:

$$ LCoE = \frac{\sum_{t=1}^{n} \frac{I_t + M_t + F_t}{(1+r)^t}}{\sum_{t=1}^{n} \frac{E_t}{(1+r)^t}} \; I_t = C_{Cap} \times \frac{r(1+r)^n}{(1+r)^n - 1} E_t = E_0 \times \left(1 - \frac{DR}{100}\right)^t \tag{16} $$

where M_t, F_t, E_t, E_0, and I_t are Operations and Maintenance (O&M) expenditures, fuel cost, electricity generation, and investment cost, respectively in year t. E_0, r, n, and DR are electricity produced in the first year of the installation, discount rate, expected lifetime of proposed power plant and degradation factor, which is assumed as 0.5% per year [18]. The main operational cost is the cost of the fuel. The remaining operation and maintenance costs have been estimated to be 5% of the total cost as suggested by Ref. [35].

The total system cost is expressed as the sum of all subsystem and installation costs as equation (17):

$$ C_{Cap} = \left(C_{MGT} + C_{Dish} + C_{Recuperator} + C_{Receiver} + C_{TES} + C_{BoP}\right) \times (1 + f_{inst}) \tag{17} $$

where $f_{inst} = 0.17$ represents installation and infrastructure costs, consistent with [17] and [38].

Each subsystem cost is parameterised as a function of its characteristic size variable, derived from literature correlations and, similar to Refs. [17], [35], [49], [55], the Chemical Engineering Plant Cost Index (CEPCI) [73] was applied to updated costs to 2024 values using equation (15):

$$ C_n = C_{ref} \times CEPCI_n / CEPCI_{ref} \tag{18} $$

which estimate the escalation of costs over the years, from the year *ref* where the known or estimated cost is C_{ref} and the index takes the value $CEPCI_{ref}$, to a year n where it is C_n and the index takes value $CEPCI_n$.

2.3.2.1. Micro gas turbine cost. To develop an updated MGT cost model capable of capturing how component-level performance characteristics influence the overall economic behaviour of the Solar–MGT system—and given the limited availability of detailed, modern cost data for small recuperated microturbines—the present work formulates the MGT subsystem cost using three complementary elements.

- The component-wise analytical expressions introduced by Galanti & Massardo [55].
- The engine cost data reported by Gavagnin et al. across twenty-four configurations, covering three mass-flow rates, two recuperator effectiveness levels, two turbine inlet temperatures, and both configurations with and without a combustion chamber [17], [74], [75].
- The subsystem cost fractions for small-scale recuperated MGTs reported in recent literature by Weerakoon et al. [64] and Abuhaiba et al. [63].

The analytical structure of equations (19)–(23) is retained to preserve the explicit dependence of compressor, turbine, combustor, generator, and recuperator costs on pressure ratio, efficiencies, mass flow rate, recuperator effectiveness.

For the cost of MGT, the approach used by Ref. [55] has been adopted and the cost of the MGT is evaluated based on the cost of each component by equations (20)–(23) and (23) for compressor, turbine, combustion chamber, generator and recuperator, respectively. To simplify the cost model, it has also been assumed that the mass flow rate of the working fluid is constant across the system and equal to the compressor inlet mass flow rate.

$$ C_{Compressor} = \frac{c_{C1}}{c_{C2} - \eta_C} \times \ln(PR_C) \times \dot{m} \tag{19} $$

$$ C_{Turbine} = \frac{c_{T1}}{c_{T2} - \eta_T} \times \ln(PR_T) \times \dot{m} \times [1 + exp(0.005 \times TIT - 6.5)] \tag{20} $$

$$C_{Combustor} = \frac{c_{CC1}}{c_{CC2} - \left(1 \Big/ \left(1 - \frac{\Delta P_{CC}}{P_{in}}\right)\right)} \times \dot{m} \qquad 21$$

$$C_{Generator} = c_{G1} \times \dot{W}^{c_{G2}} \qquad 22$$

$$C_{Recuperator} = 1.5 \times c_{R1} \times f \times \dot{m} \times \left(P_{in} \times \Delta P_{Recuperator}\right)^{-0.5} \times \frac{\varepsilon}{1-\varepsilon} \qquad 23$$

$$C_{Power\ Electronics} = c_{PE1} \times \dot{W}^{c_{PE2}} \qquad 24$$

In these equations PR_C, PR_T, $\dot{m}$, η_C, η_T, ΔP_{CC}, $\dot{W}$, $\Delta P_{Recuperator}$, and ε are the compressor and turbine pressure ratio, compressor mass flow rate, compressor isentropic efficiency, turbine isentropic efficiency, combustor pressure loss, system electric output power, combustor pressure loss (cold path), recuperator pressure loss (maximum of hot and cold sides) and recuperator effectiveness, respectively, which are defined in the previous section. The updated c_x coefficients in these equations are presented in Table 4. Parameter f in recuperator cost function is the material cost factor which reflect the material that can be used in manufacturing of the recuperator that limits the maximum allowable temperature of the recuperator (Table 5).

A comparison between the recalibrated cost model and the MGT cost values reported by Ref. [17] is presented in Fig. 3-a. The results show that the updated coefficients accurately reproduce the reference costs across different configurations, covering variations in mass flow rate, TIT, and recuperator effectiveness. To examine the feasible internal allocation of costs among subsystems of the present model, Fig. 3-b shows the component costs from the recalibrated model (averaged over the 12 operating points used in Fig. 3-a) against the hardware cost fractions reported for small recuperated microturbines by Weerakoon & Assadi, 2024 [64]. Fig. 3-b therefore provides an external verification of the subsystem cost distribution, showing the relative contributions of turbomachinery, combustor, recuperator, and electrical components. Enclosure and balance-of-plant costs, which are treated separately at the system level in this work, were excluded for consistency with the literature. The comparison demonstrates that the recalibrated cost model yields a component-level structure that is consistent with published data for small-scale MGTs, reinforcing the physical realism of the updated coefficients.

2.3.2.2. Solar dish and receiver. The cost of the solar dish makes up the largest portion of the overall plant cost [15], [38]. The dish cost is primarily determined by its surface area and the complexity of its tracking mechanism. For this study, the tracking mechanism has been assumed to be consistent across configurations. The cost of the solar dish is estimated using a common equation based on the works of [17], [34], [35] as shown in equation (25).

$$C_{Dish} = c_{Dish} \times A_{Dish}{}^{n} \qquad 25$$

Iaria et al. [35] used a linear relationship between the dish cost and its area assuming a constant value for the c_{Dish} as 260 €/m^2. Gavagnin et al. [74] evaluated the cost of collector dishes ranging from 50 to 210 m^2 using manufacture and adopted a quadratic polynomial to the c_{Dish} assuming $n = 1$ that shows specific cost of the dish decreases for increasing aperture area but, from a certain size on (about 100 m^2), it increases again. Similar approach has been adopted to the current research, assuming $n = 1$ and c_{Dish} as equation (26):

$$c_{Dish} = a_{2,Dish} \times A_{Dish}{}^2 + a_{1,Dish} \times A_{Dish} + a_{0,Dish} \qquad 26$$

Table 5
Material cost factor and maximum allowable material for different recuperator materials [55].

Material	Stainless steel	Super 347	Inconel 625	Haynes 230	Haynes 214
Maximum metal Temperature [K]	948	1023	1073	1123	1173
f	1.0	1.5	5.0	7.0	9.0

where $a_{2,Dish}$, $a_{1,Dish}$ and $a_{0,Dish}$ are updated for small production to 2024 values as 0.0064, −1.25 and 425, respectively. In the present implementation, the dish cost and optical-efficiency assumptions are applied within the selected dish-area range of the parametric study. Application to substantially larger concentrators would require recalibration of both the dish cost correlation and the optical-performance sub-model.

The receiver cost is influenced by several factors, including its capacity and its operating temperature. The latter impacts material and manufacturing expenses which is not considered in this model, for the sake of simplicity. To estimate the cost of the receiver based on its capacity, the cost function was derived from a study by Gavagnin et al. [17] for a cavity receiver in the OMSoP project. This study accounted for direct labour, material, and manufacturing costs. Based on the results, an interpolation was performed, leading to equation (27), which expresses the receiver cost as a function of the absorbed heat.

$$C_{Receiver} = c_{Receiver} \times Q_{Receiver}{}^{0.6} \qquad 27$$

where $c_{Receiver}$ is set as 124.0 €/kW of receiver thermal capacity.

2.3.2.3. Thermal energy storage. Phase change material type is considered as thermal energy storage in this research. The cost of the energy storage is related to its capacity and material. A linear correlation is used in this study to calculate the cost of storage system based on its energy capacity (equation (28)).

$$C_{TES} = c_{TES} \times E_{TES} \qquad 28$$

where the E_{TES} is the thermal energy capacity of the TES and the c_{TES} is the specific cost per unit of energy. The specific cost itself varies for different materials. Table 6 lists the characteristics and specific cost of different phase change material with different melting temperature. An interpolation was performed over this data and a linear regression of equation (29) was defined to calculate the specific cost.

$$c_{TES} = 0.20 \times T_m[K] - 90 \qquad 29$$

In which T_m is the phase change temperature and c_{TES} is the specific cost in €/kWh.

2.4. Simulation approach

The thermodynamic and economic models described above were integrated into an annual simulation framework implemented in MATLAB, enabling the coupled evaluation of system performance and cost across a full year of operation under realistic meteorological conditions. The simulation follows a quasi-steady time-marching structure, resolving the system response to hourly variations in ambient conditions and solar irradiance while maintaining internal mass- and energy-balance closure at each time step.

The DNI, ambient temperature, and pressure data for Pretoria, South

Table 4
Coefficients of the micro gas turbine and recuperator cost function based on [55] updated for 2024.

Cost coefficient	c_{C1}	c_{C2}	c_{T1}	c_{T2}	c_{CC1}	c_{CC2}	c_{G1}	c_{G2}	c_{R1}	c_{PE1}	c_{PE2}
Value	82.6	0.942	371.6	0.903	83.7	0.995	125.3	0.8	376	1100	0.2

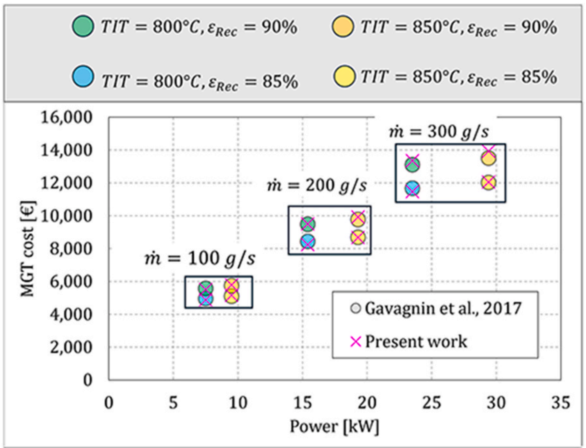

(a)

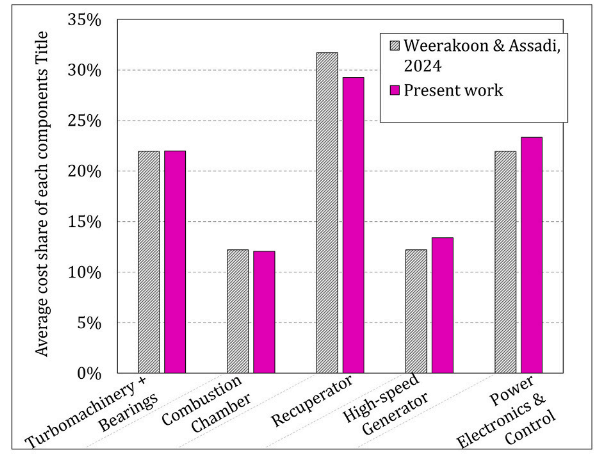

(b)

Fig. 3. Verification of the recalibrated MGT cost model; (a) Comparison with engine-only cost values reported by Ref. [17] across multiple operating conditions; (b) subsystem cost-share comparison with [72], excluding enclosure/BoP.

Table 6
Specific costs of thermal energy storages with different phase-change materials based on [48] and [49], updated for 2024.

Phase-change material	Melting temperature [K]	Latent heat, L_f [kJ/kg]	Cost per kWh of stored thermal energy (€/kWh)
H425	698	220	38
Zinc	692	112	34
Solar salt	495	100	5
Cu-Si (83-17)	1075	267	122
Al-Cu-Si (2-83-15)	1036	258	125

Africa, were obtained from the Southern African Universities Radiometric Network (SAURAN [67]). The input data set covers an entire calendar year and provides the environmental boundary conditions for the solar receiver, compressor inlet, and TES heat losses. Each simulation step evaluates the instantaneous thermal power input, component states, and resulting electrical output, which are then aggregated to produce the annual performance indicators.

At each time increment, the following sequence is executed.

1. Meteorological update: Read DNI, T_{amb}, and P_{amb} for the current hour. Compute the corresponding solar power incident on the dish.
2. Receiver and TES interaction: Determine the portion of solar energy absorbed by the receiver and transferred to the TES according to equation (12). The TES operating mode (charging, discharging, or idle) is automatically identified from equation (11).
3. MGT off-design solver: Using the current TES outlet temperature and receiver input, the MGT thermodynamic solver computes component temperatures, pressures, and mass flow rates, adjusting turbine and compressor efficiencies from off-design maps. Off-design operation is implemented by maintaining a constant turbine inlet temperature (TIT); fuel flow is iterated until the target TIT is achieved. The resulting turbine outlet temperature and net electrical output are then determined.
4. Energy accounting: Net power output, recuperator heat exchange, system losses, and TES energy variation are calculated.
5. Economic accumulation: Hourly electrical output E_t and fuel consumption $\dot{m}_{Fuel}$ are logged and accumulated to compute annual totals for use in the LCoE evaluation (equation (16)).

The process is repeated for each parametric configuration, defined by a unique combination of TIT, EGT, solar dish area, TES mass, and recuperator effectiveness, allowing direct quantification of how each variable affects both performance and cost metrics.

Convergence of the simulation is ensured through nested iteration: the inner loop balances compressor–turbine work and mass flow, while the outer loop matches thermal inputs and outputs over the entire system boundary.

The overall simulation workflow is summarised in Fig. 4, which illustrates the coupling between the thermodynamic solver, TES dynamics, and cost post-processing modules.

2.5. Model verification and validation

Verification focused on ensuring numerical accuracy, thermodynamic consistency, and proper implementation of the governing equations. Due to the lack of modern, fully documented Solar–MGT cost breakdowns including TES and high-speed power electronics, the verification of the cost model was presented at the microturbine level in the previous section, while system-level validation is focused on thermodynamic performance.

Model validation was performed in two stages to assess the accuracy and robustness of the developed simulation platform. In the first stage, experimental data from a recuperated MGT operating under multiple full- and part-load conditions were employed to tune (based on test data at 15 °C and 150 kRPM) the MGT component and verify the model across a broad range of operating points. In the second stage, limited experimental data from one of the configurations tested at the University of Pretoria (South Africa) were used to validate the integrated solar-assisted configuration within the framework of the *Solar Turbo CHP* project using the data published in Ref. [66].

A schematic of the experimental test cell and measurement setup is shown in Fig. 5. The MGT is integrated with a costume-build recuperator with UA = 125 W/K. Details of the experimental set-up can be found in Ref. [52]. Off-design simulations were conducted to evaluate performance under varying ambient conditions.

Fig. 6 presents the model predictions and experimental measurements for (a) output power and (b) the recuperator air-side outlet temperature. The experimental temperature range during testing was 11–19 °C. The simulated trends closely follow the expected thermodynamic behaviour of micro gas turbines. The maximum deviation in power output was below 3% at 11 °C. Slightly higher discrepancies at lower ambient temperatures were attributed to increased heat losses in the recuperator and associated piping. This is reflected in turbine outlet temperature differences of up to 4 °C and air outlet temperature deviations below 6 °C, (see Table 7). The model's accuracy was further assessed by analysing the effect of shaft speed on power output and fuel

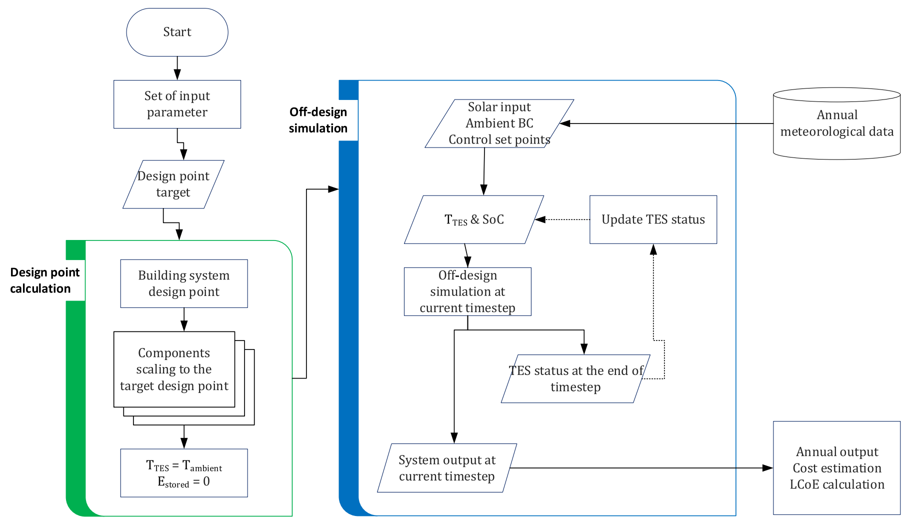

Fig. 4. Simulation workflow.

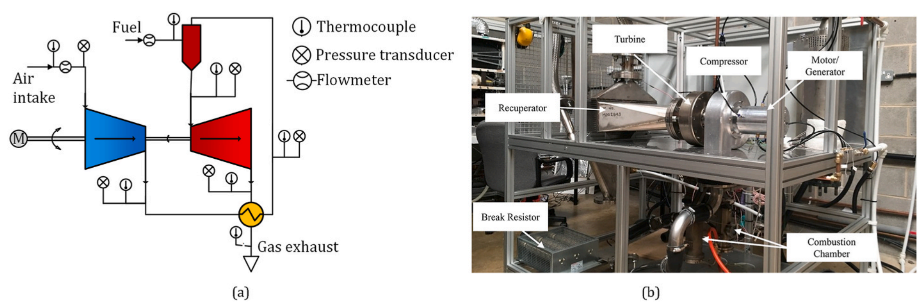

Fig. 5. Test arrangement of the recuperated micro gas turbine and associated sensor positions [52].

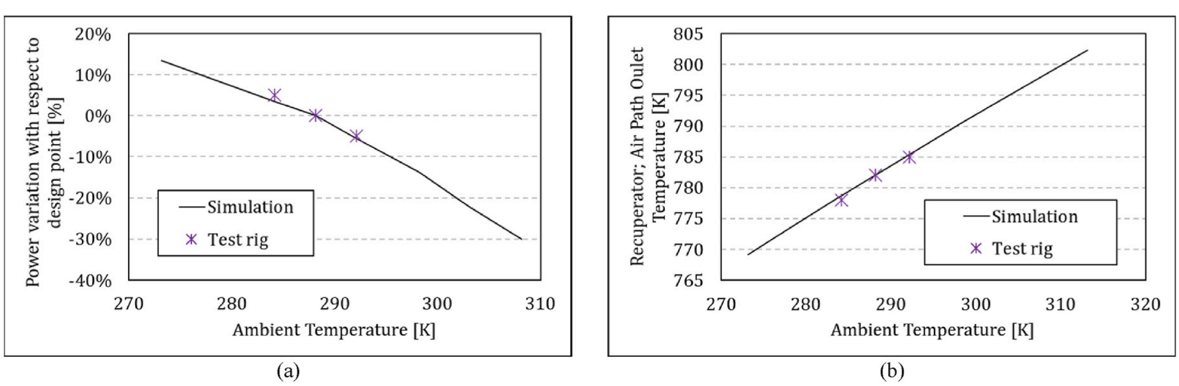

Fig. 6. Off-design comparison of model predictions and experiments: effect of ambient temperature on (a) power output, (b) air-path recuperator outlet temperature.

consumption, as illustrated in Fig. 7. With a constant turbine inlet temperature, the simulation accurately reproduces the experimental trends. The maximum deviations were 18% for power output and 20% for fuel consumption, confirming the model's capability to predict performance variations with speed.

For the solar-assisted configuration, experimental data from a dish-integrated micro gas turbine (MGT) system were used for model validation (Table 8). The experimental data were obtained from the solar dish–Brayton prototype developed within the Solar Turbo–CHP project at the University of Pretoria (Fig. 8-a), described in detail by Refs. [52], [66]. The system integrates a similar MGT introduced earlier, with a high effectiveness recuperator and a 24.75 m^2 parabolic dish concentrator. A fuel-supply line (LPG) provides supplementary combustion to maintain the desired turbine inlet temperature.

Fig. 8-b presents the measured temperatures and experimental results. As reported in Swanepoel et al., 2024, the test started at 13:45, by focusing the solar dish reflectors to the receiver. The system went through initial checks and warm-up process to 15:00. The data indicate that after initial transients, the system approached a near steady-state condition between 16:46 to 16:48, marked in Fig. 8-b as the point of interest (POI). Fig. 9-a and –b show the comparison between the experimental measurement with the simulation output for the receiver inlet and receiver outlet, respectively. As the model does not include the thermal inertia and other dynamics of the system, there is a visible gap between the results during initial warm-up and DNI sudden changes. Apart from these, the results show good agreement, with deviations

Table 7
Off-design modelling assumptions for MGT validation.

Parameter	Initial Design Point	Test-cell Design Point (calibrated)	Off-design point 1	Off-design point 2	Off-design point 2	Unit
Ambient temperature	288	288	284	288	292	K
Ambient pressure	1.0132	1.0132	1.022	1.022	1.022	bar
Rotational speed	150	150	137	137	137	kRPM
Air mass flow	0.100	0.100	0.079	0.078	0.077	kg/s
Compressor pressure ratio	2.99	2.88	2.71	2.68	2.65	–
Compressor efficiency	0.73	0.73	0.7	0.71	0.69	–
Recuperator effectiveness	87%	60.0%	60.1%	60.2%	60.4%	–
Turbine inlet temperature	1150	1150	1150	1150	1150	K
Turbine pressure ratio	2.68	2.56	2.38	2.35	2.33	–
Turbine efficiency	0.7	0.63	0.64	0.63	0.63	–
Electric output power	5.307	3.001	2.255	2.165	2.027	kW

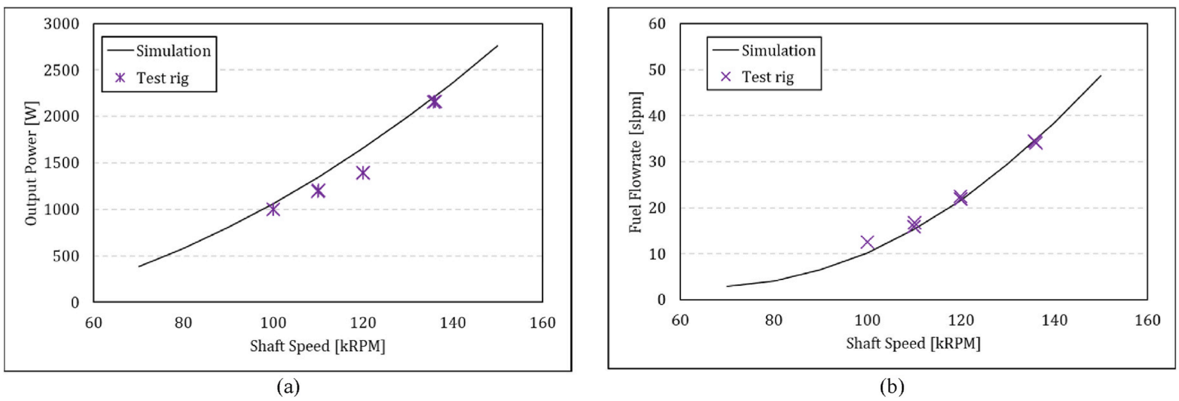

Fig. 7. Off-design validation comparing predicted and measured performance: (a) power output and (b) fuel flow at different shaft speeds.

Table 8
Experimental conditions used for model validation, extracted from [66].

Parameter	Value	Unit
Recuperator effectiveness	80%	–
Solar dish area	25	m^2
Intercept factor	0.67	kg/s
Receiver emissivity	0.72	m^2
Receiver outer area (sides)	4 × 0.293	–
Receiver outer area (top)	0.169	m^2
Receiver outer area (back)	0.106	m^2
LHV of LPG	95790	kJ/kg

below 50 K across a 1000 K temperature range. These differences fall within experimental uncertainty and confirm that the developed model accurately captures the solar system contribution.

3. Results and disscussion

The integrated thermodynamic and economic simulations were performed using the verified model under the climatic conditions of Pretoria, South Africa. The DNI and ambient-temperature data from SAURAN [67] were used to compute annual performance and cost metrics across the parametric space defined by TIT, EGT, solar dish area, TES mass and temperature, and recuperator effectiveness. Unless stated otherwise, the baseline configuration is assumed as values presented in Table 9.

While the analysis is conducted over a full-year dataset, selected representative daily profiles (Figs. 10–12) are presented only to illustrate the transient behaviour and resolution of the model. All techno-economic indicators and performance metrics are derived from annual integrated results.

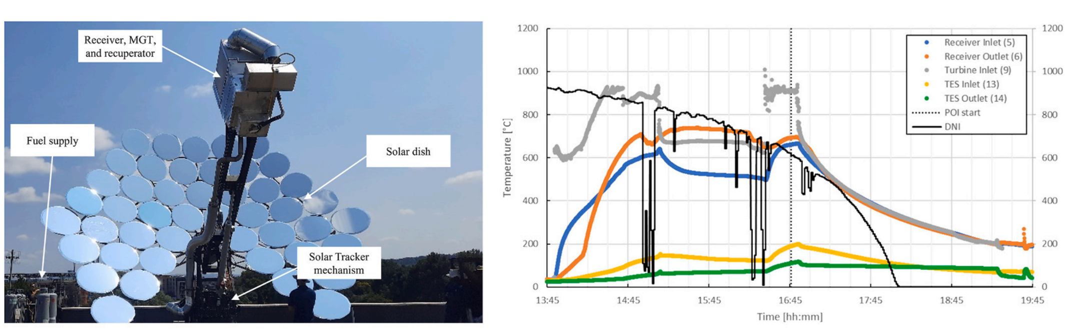

Fig. 8. Solar MGT demonstration arrangement of the project "Solar Turbo CHP", Pretoria, SA: (a) demonstration prototype [52], (b) experimental test result of the dish MGT system, reprinted from [66], with permission from Elsevier.

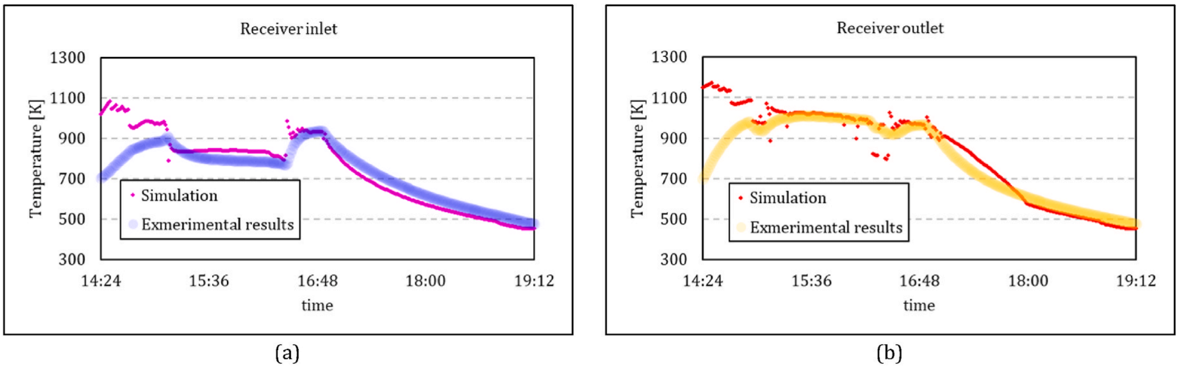

Fig. 9. Comparison of measured and simulated receiver temperatures: (a) inlet temperature, (b) outlet temperature.

Table 9
Main design specifications of the base-case system.

Item	Value	Unit
Turbine Inlet Temperature	1150	K
Exhaust Has Temperature	1000	K
Compressor mass flow rate	0.080	kg/s
Solar dish area	30	m^2
TES mass	400	kg
TES material melting temperature	1000	K
Recuperator UA	0.272	kW/K

3.1. System operation overview

The baseline simulation was first analysed to understand the integrated behaviour of the hybrid system over representative days and full year. As shown in Fig. 10, the system provides continuous electrical power through hybrid operation. During daylight hours, the dish–receiver combination supplies most of the thermal input, with TES absorbing excess heat during peak DNI. When solar input decreases, stored heat is discharged to preheat the compressed air, reducing the need for fuel. This integration of TES mitigates transients associated with cloud fluctuations and reduces the load changes on combustion chamber.

The annual fuel-to-electric efficiency reaches 16–17%, with a solar contribution of about 18% of the total energy input. The TES discharge

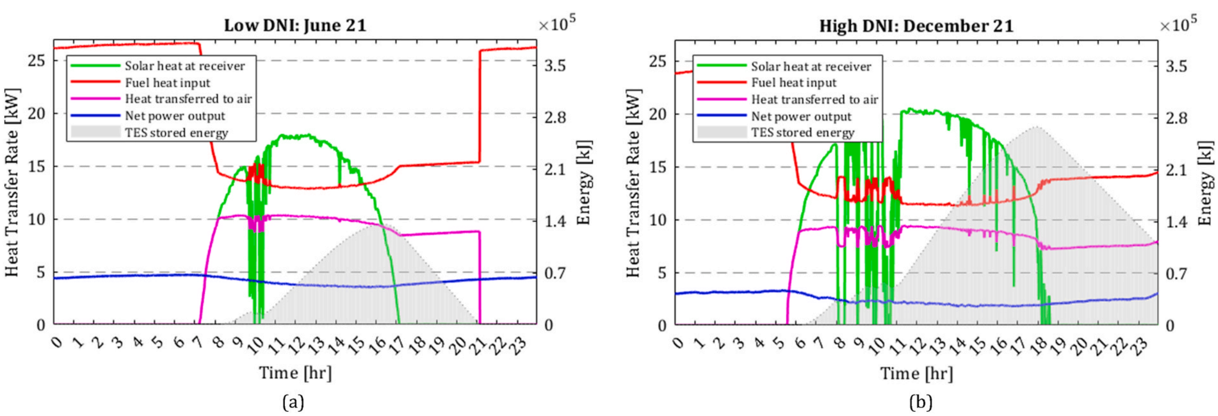

Fig. 10. Heat balance of the receiver and energy content of the TES at the base point (1000 K): (a) Low DNI day (June 21), (b) High DNI day (December 21).

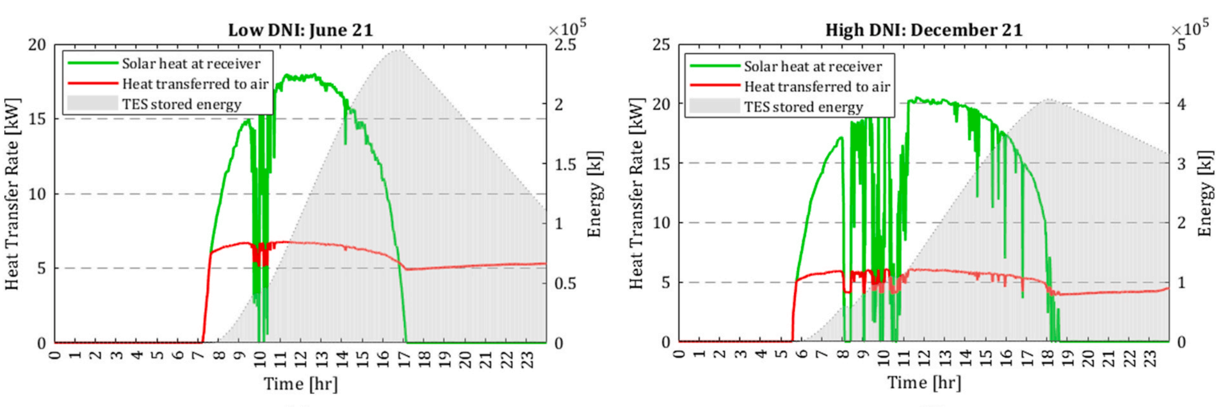

Fig. 11. Heat balance of the receiver and energy content of the TES at 950 K: (a) Low DNI day (June 21), (b) High DNI day (December 21).

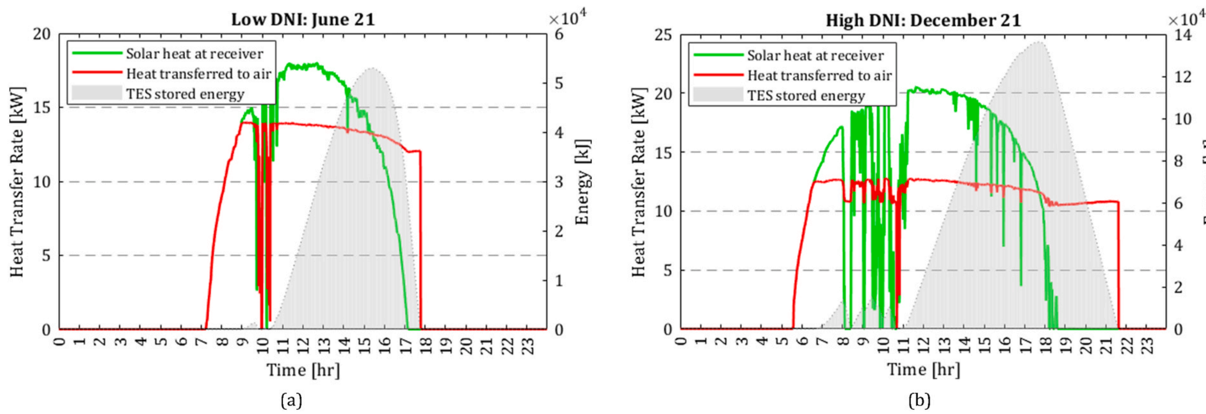

Fig. 12. Heat balance of the receiver and energy content of the TES at 1050 K: (a) Low DNI day (June 21), (b) High DNI day (December 21).

assist the system operation about 1400 h of the year, increasing the average daily operation time of solar-assisted mode by approximately 3.8 h. These results demonstrate the capability of the TES to maintain stable output and extend solar utilisation during off-peak hours.

3.2. Effect of TES working temperature

TES parameters have the most pronounced combined impact on both technical and economic performance. Incorporating a low temperature TES indeed increases the amount of stored thermal energy. The heat transfer balance is illustrated for lower and higher TES temperatures in Figs. 11 and 12, respectively. Using a material with a lower melting point reduces the heat transfer capacity between the TES and the incoming working fluid (outlet of the recuperator cold path). Consequently, the TES remains charged by the end of the day on both low and high DNI days, as seen in Fig. 11. Conversely, increasing the TES temperature enhances the heat transferred to the working fluid but also results in greater heat losses due to radiation and convection. As depicted in Fig. 12, with a TES melting temperature of 1050 K, the TES cannot fully compensate for early fluctuations in solar input and becomes fully discharged on both representative days.

With low-temperature storage, excess solar energy can be stored during high DNI days and used on low DNI days. However, this strategy of storage requires storage capacity exceeds 3–4 times the base-case daily storage demand, corresponding to a PCM mass on the order of 10^3 kg for typical latent heat values, making it impractical for small-scale systems. Therefore, a thermal capacity limit of $1.6\times\ 10^5 kJ$ is set for the TES. This value corresponds to the storage energy required to compensate for the thermal deficit on a representative low-DNI day at the base TES operating temperature and is used as a practical upper bound for annual performance evaluation. Fig. 13 shows the annual fuel-to-electric efficiency of the based on different values of the TES temperature. It is observed that as the TES temperature increases from 950 K to around 1050 K, the fuel-to-electric efficiency improves, peaking at a temperature close to TIT, 1045 K for the base point (TIT = 1150 K). However, the marginal benefit declines beyond this range due to additional storage loss of the high temperature material during its idle periods. It reaches 17% at 1150 K for the base design and indicates that there is an optimal TES temperature range where the system achieves the highest fuel-to-electric efficiency. This temperature is related to the size of the sub-system and the inlet temperature of the TES (recuperator outlet temperature at cold path) and TIT set point.

Utilising a TES with higher temperature requires more expensive materials, which increase the equipment cost, Fig. 14-a. It is, however, makes it possible to use less amount of PCM material for storage, which reflected to the reduction of the cost after a certain temperature (1075 K for the base design). The Levelised Cost of Electricity, which combines both performances and cost is plotted in Fig. 14-b showing an oscillating

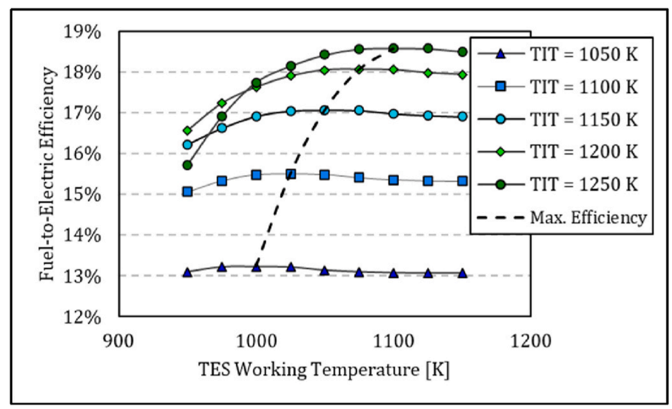

Fig. 13. The effect of TES working temperature on system overall performance: annual efficiency with different TIT set points.

behaviour. The relative variation, (maximum value – minimum value)/average value, increases from 4.7% to 13.4% for TIT = 1050 K to TIT = 1250 K, respectively. While the absolute values of LCoE are subject to modelling uncertainty, the observed trend and relative variation with TES temperature remain consistent. In all cases the TES material should be chosen to have a melting temperature close to the target TIT to achieve the lowest LCoE. These results confirm that the TES design should target moderate temperature to maximise system-level cost-effectiveness. Using the component-based techno-economic model can simulate the combined effect to find the optimum design for each set-up.

The TES working temperature governs annual performance through a coupled thermodynamic–utilisation mechanism. Low discharge temperature reduces the effective heat-transfer driving potential to the recuperator outlet stream, limiting how much stored energy can be converted into useful preheating and therefore limiting annual fuel displacement under the constant-TIT control strategy. As TES temperature increases toward the TIT set point, the discharge becomes more effective and the annual fuel-to-electric efficiency increases, reaching a maximum when TES temperature is close to the effective preheat requirement (e.g., ~1045 K for the base point, Fig. 13). Beyond this range, the marginal benefit declines because higher-temperature storage experiences greater standing losses during idle periods and because specific PCM cost rises sharply with melting temperature (Table 6), which dominates the LCoE response (Fig. 14). The combined outcome is that TES temperature has an identifiable techno-economic optimum: it must be high enough to deliver useful preheat at the chosen TIT, but not so high that loss exposure and material cost outweigh incremental fuel savings.

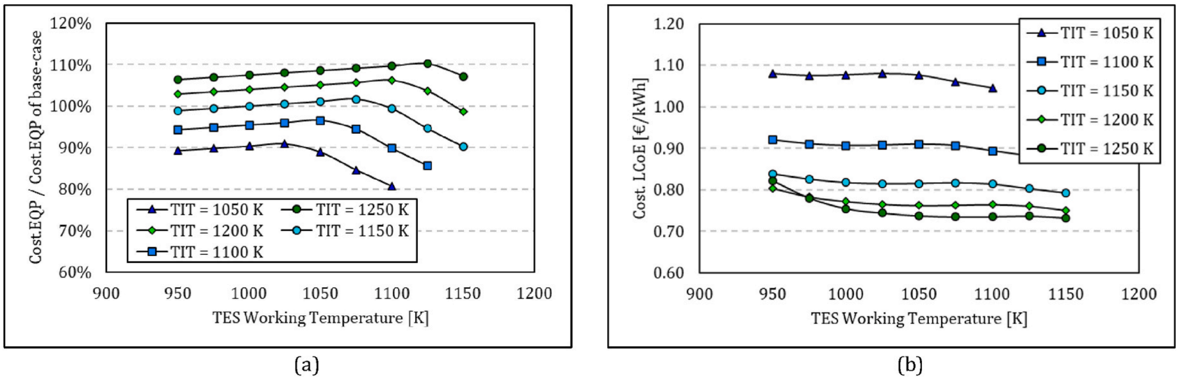

Fig. 14. The effect of TES working temperature on the overall cost metrics of the system: (a) total equipment cost, (b) LCoE.

3.3. *Effect of recuperator characteristics*

Recuperator effectiveness significantly influences both system efficiency and cost. Increasing effectiveness reduces fuel consumption by enhancing exhaust heat recovery, but at the expense of higher capital cost.

Fig. 15-a shows the effect of recuperator effectiveness on changes on annual fuel consumption and energy generation. With higher effectiveness, more energy is recovered from the turbine exhaust which results in less fuel consumption. However, a higher effectiveness requires large heat transfer area, which increases capital cost of the recuperator, and leads to higher pressure loss, resulting in lower net power output. Combining these two effects, Fig. 15-b illustrates the relationship between design-point effectiveness and Fuel-to-Electric Efficiency of a system. Since the effect of the reduction in fuel consumption is considerably greater that reduction of energy generated for higher effectiveness values (Fig. 15-a), the graph shows a positive near linear trend in improvement of the fuel-to-electric efficiency. Pressure loss is not the only penalty of a recuperator with a higher effectiveness value. As can be seen in Fig. 16, expectedly, increases the cost of the recuperator and the system. However, accompanying with higher system efficiency (less O&M cost due to less fuel consumption), it enhances the overall LCoE from 0.90 €/kWh at effectiveness of 77% to 0.81 €/kWh at 91%, which translates to 10% improvement. The figure shows that this non-linear effect is not monotonous and as total generated electricity of the system is decreasing sharply with high pressure loss values accommodated with high effectiveness values (Fig. 15-a).

Recuperator effectiveness affects LCoE through two competing channels that act on different denominators of the LCoE expression: it reduces annual fuel consumption by increasing preheat temperature (lowering required combustor heat addition to maintain TIT), but it simultaneously penalises net electricity generation through increased pressure losses and raises CAPEX through larger heat-transfer surface area (Figs. 15 and 16). The results show that, over most of the investigated range, the fuel-saving benefit dominates the electricity-loss penalty, producing a near-linear improvement in fuel-to-electric efficiency (Fig. 15-b). The slight non-monotonic behaviour at high effectiveness is

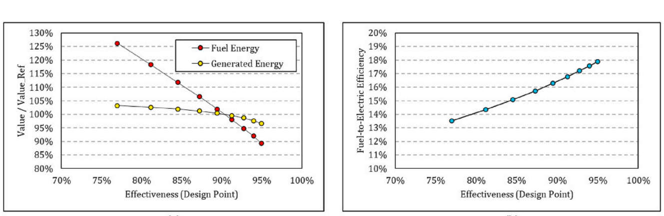

Fig. 15. The effect of recuperator effectiveness on the annual performance of the system: (a) consumed fuel and generated electricity, (b) fuel-to-electric efficiency.

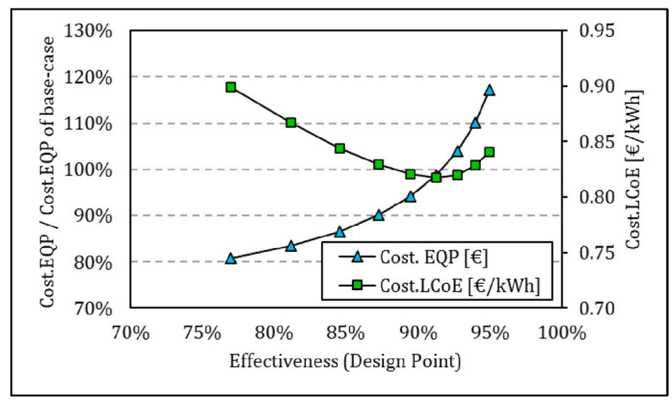

Fig. 16. The effect of recuperator effectiveness on the total equipment cost and LCoE.

physically consistent with pressure-loss amplification: once pressure losses drive a sharp reduction in annual energy output (Fig. 15-a), the reduced denominator in LCoE limits further economic improvement even if fuel continues to fall. This explains why maximising effectiveness is not automatically optimal as it is the fuel-saving-to-power-loss ratio, weighted by component cost, that governs the economic outcome.

3.4. *Effect of solar dish area*

Increasing the solar dish area proportionally increases the absorbed solar thermal input, thereby reducing the required fuel flow. This effect is more pronounced at lower TIT values, where the baseline fuel demand is smaller and the solar contribution represents a larger fraction of the total thermal input. At higher TIT, the increased receiver temperature results in higher radiative losses, which partially offset the additional solar input. Therefore, the effect on fuel-to-electric efficiency is more pronounced at lower TIT values, Fig. 17. For a specific TES arrangement (Fig. 17-a), increased solar input is stored or diminish as a heat loss in receiver and TES. Consequently, the efficiency improvement becomes marginal for TIT>1150 K.

As it was discussed on Fig. 13, for any specific arrangement of solar dish and TIT, there is an optimum temperature for the TES in which the Fuel-to-Electric efficiency reaches its maximum value. Using this TES arrangement for each TIT case results in a near-liner increase in efficiency in all Tit cases (Fig. 17-b). The MGT-TES combination has a limited capacity to utilise the input heat which limits the performance improvement from TIT = 1200 K to TIT = 1250 K as shown approximately overlapping results in Fig. 17-b.

The solar dish has been identified as the primary cost component in dish-MGT systems ([17], [38], [71]), and any increase in its cost

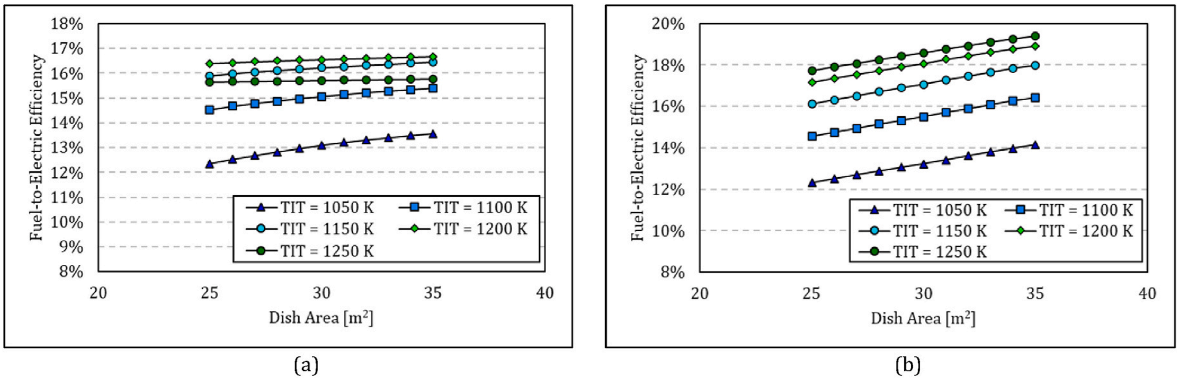

Fig. 17. The effect of dish area on the annual performance (Fuel-to-Electric Efficiency) system with different TIT: (a) base design TES temperature, (b) TES temperature at optimum performance (Fig. 13).

substantially raises the total equipment expenditure (Fig. 18-a). In the base design configuration, enlarging the dish area from 25 to 35 m^2 reduces fuel consumption and increases the solar energy contribution to overall power generation by up to 40% over a full annual cycle (24 h $\times$ 365 days). This escalation in capital expenditure leads to a reduction in the LCoE only when an appropriately sized TES system is selected; however, the resulting LCoE reduction remains modest under current fuel and electricity pricing conditions in SA (Fig. 18-b).

Dish area influences annual LCoE predominantly through a CAPEX-dominated fuel-displacement pathway. Technically, larger area increases absorbed solar heat, reducing fuel required to hold TIT, but the marginal efficiency gain decreases at higher TIT because elevated receiver temperatures increase radiative loss and because additional solar heat increasingly shifts into storage/thermal losses rather than incremental fuel displacement (Fig. 17-a), making efficiency improvement marginal for TIT $\gtrsim$ 1150 K in the base TES arrangement. When TES temperature is tuned to the efficiency-optimal value for each TIT case, the efficiency trend becomes closer to linear (Fig. 17-b), but the results still indicate a utilisation ceiling where the MGT–TES path cannot convert additional thermal input into proportional annual efficiency gain. Economically, dish cost dominates small dish-MGT CAPEX (Fig. 18-a), so increasing area produces a substantial cost increase while the fuel savings saturate; hence LCoE reductions remain modest under the assumed South African price structure, even though solar contribution can rise markedly.

The smooth trends observed over the investigated dish-area range therefore describe the local behaviour of the present small-scale Solar-MGT configuration. For substantially larger concentrators, the useful solar input does not scale only with aperture area, since the effective dish optical efficiency can also become size-dependent. Recent optical-mechanical studies of large dish/Stirling systems have shown that self-weight deformation and wind loading can influence mirror slope error, receiver flux distribution and optical efficiency [76], [77]. Extending the present dish-area trends to large-aperture systems would require recalibration of the optical-performance and cost models, together with redesign of the receiver, storage and MGT subsystems.

3.5. *Effect of MGT mass flow*

The mass flow rate reflects the overall size and capacity of the MGT and has a significant influence on system performance, including power output, fuel consumption, and sensitivity to variations in solar input. Turbomachinery performance maps are scaled as described in Section 2.3.1, which captures size-related efficiency variation within the same technology family. Increasing the mass flow rate generally enhances the power output but may also raise fuel consumption, potentially offsetting the benefits of higher solar contribution. As shown in Fig. 19, the fuel-to-electric efficiency decreases with increasing mass flow rate, since a fixed solar input results in a smaller temperature rise in the solar receiver. Consequently, additional fuel is required in the combustion chamber to achieve the target TIT, thereby reducing efficiency beyond the optimal mass flow range. The observed decline in fuel-to-electric efficiency across various configurations, as shown in Fig. 19, confirms the validity of the developed model over a wide range of operating conditions. For a given dish area, the temperature rise in the receiver increases with lower mass flow rates, which leads to greater thermal losses. Additionally, the heat transfer rate to the thermal energy storage (TES) unit rises, resulting in increased energy losses within the TES. Consequently, the fraction of solar heat effectively transferred to air does not increase proportionally with mass flow rate (Fig. 20-a). As a result, the overall fuel-to-electric efficiency is higher at lower mass flow rates. Furthermore, with a fixed recuperator design, its effectiveness decreases as the mass flow rate increases (Fig. 20-b), further contributing to efficiency deterioration.

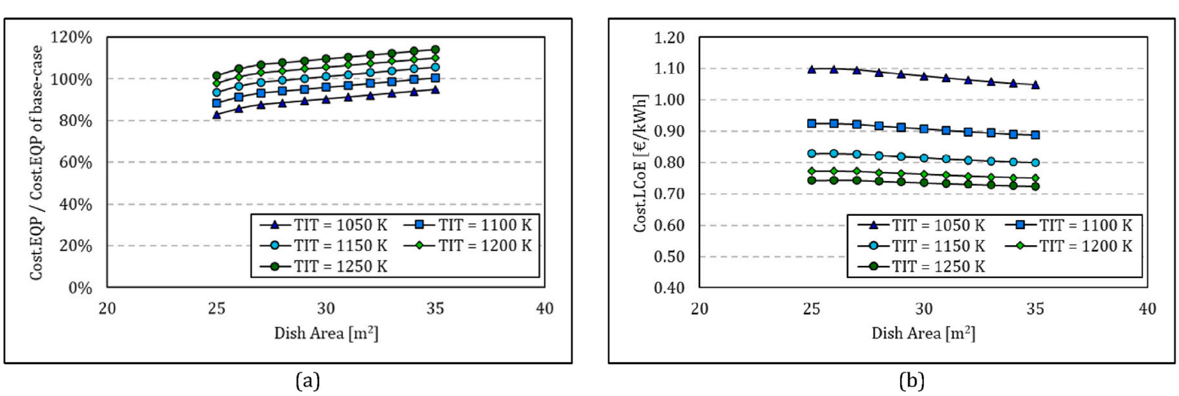

Fig. 18. The effect of dish area on the overall cost metrics of the system for the optimum TES temperature scenarios: (a) total equipment cost, (b) LCoE.

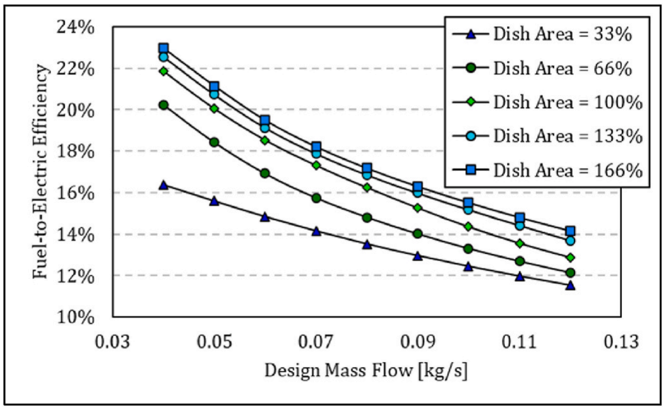

Fig. 19. The effect of mass flow rate on the annual performance (Fuel-to-Electric efficiency) of system with different dish sizes.

Economically, higher mass flow also implies a larger nominal MGT (and therefore higher component CAPEX), but unless the additional electricity generation is accompanied by proportional fuel savings, the LCoE improvement is limited; Overall, it can be concluded that for each system configuration, there exists an optimal mass flow rate at which the thermal-power efficiency reaches its maximum value.

3.6. Summary of the parametric study

The effects of the major design parameters on the performance and cost of the Solar-MGT system have been discussed in detail in this section, providing both a demonstration of the modelling capability and a clear picture of individual parameter sensitivities.

MGT-side parameters influence annual LCoE through their sustained impact on Brayton-cycle thermal efficiency and specific fuel consumption across the full operating year. Increasing mass flow, increase the output power, and increasing TIT or recuperator effectiveness directly increases cycle efficiency, reducing fuel input not only during high-DNI operation but also during low-solar or TES-depleted periods. Because fuel cost contributes continuously to operating expenditure, efficiency-driven reductions translate into disproportionately strong annual economic leverage, even when associated component costs increase. This explains why turbine-side improvements tend to produce larger and more consistent LCoE reductions compared with solar-side changes under the same operating assumptions.

In contrast, the economic leverage of the solar-field and TES variables is governed primarily by net annual fuel displacement per unit added CAPEX, i.e., how much of the additional solar heat becomes useable preheat under the TIT-controlled operating strategy. Increasing dish area raises absorbed solar input and therefore reduces fuel demand, but the annual efficiency benefit is progressively moderated by two coupled effects evident in the results: (i) receiver heat losses increase strongly with operating temperature, so the marginal conversion of additional solar input into useful cycle heat decreases at higher TIT, and (ii) the receiver–TES–MGT thermal pathway exhibits a utilisation ceiling, such that further solar input increasingly manifests as TES charging and loss exposure rather than proportional additional fuel displacement. But higher TES temperatures lead to diminishing or adverse economic returns because specific PCM cost rises sharply with melting temperature and because higher-temperature storage experiences greater standing-loss exposure. Consequently, dish enlargement and TES upgrades tend to deliver their strongest benefit when they increase useable solar utilisation over the year, whereas their LCoE impact remains comparatively modest when additional solar input is limited by loss mechanisms and cost–temperature constraints.

The objective here is to identify which parameters offer the highest potential for improving overall system performance. Since different parameters influence system behaviour with different magnitudes, the variations were selected such that each scenario corresponds to a similar increase in system CAPEX relative to the base design.

Fig. 21 summarises the comparative results for five design-improvement scenarios: increased system capacity (increase air mass flow by 40%), improved turbomachinery efficiency (by 17% relative), improved recuperator effectiveness (by 15% relative), increased operating temperature (both turbine and TES, by 150 K), and increased dish area (by 10%). As shown in Fig. 21-a, enhancements in turbomachinery efficiency and recuperator effectiveness provide the largest gains in fuel-to-electric efficiency, while solar share increases most when recuperator effectiveness or dish area is improved.

The techno-economic impact is presented in Fig. 21-b through a trade-off map between annual electricity generation and LCoE. Although all scenarios assume a comparable CAPEX increment, their LCoE response differs substantially. Improvements in turbomachinery and recuperator effectiveness deliver the largest reduction in LCoE, although only the former is accompanied by a substantial increase in annual electricity generation. Increasing system capacity and operating temperature improve annual output, but with more modest economic benefit, while increasing dish area has almost no effect on annual electricity generation and only a marginal influence on LCoE in this comparison. Overall, these results show that efficiency-driven upgrades yield the strongest combined performance and cost advantage, whereas solar-collection enhancements primarily improve solar utilisation. Crucially, the earlier parametric analysis demonstrated that these trends are mainly nonlinear; thus, different magnitudes of improvement could shift the balance between fuel-driven and solar-driven gains, potentially altering the relative benefit of each design pathway.

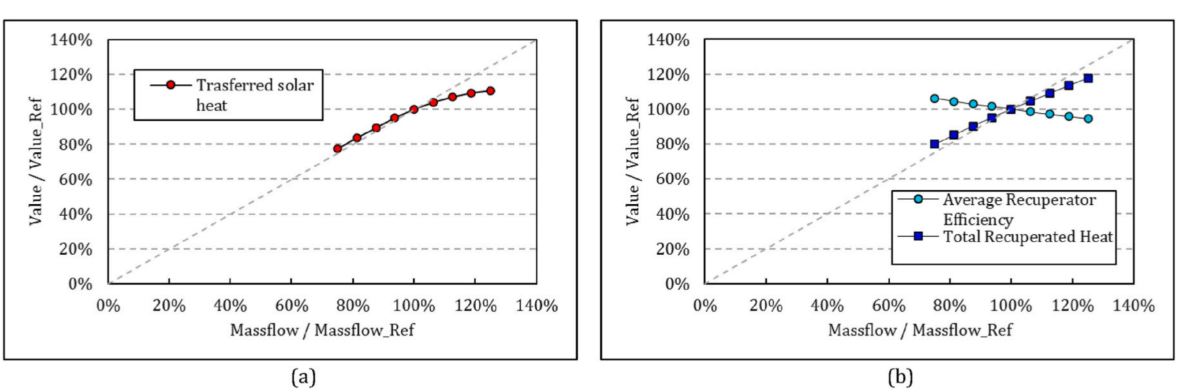

Fig. 20. The effect of mass flow rate on subsystem performances: (a) heat transfer to working fluid form solar source (b) average recuperator effectiveness and total recuperated heat.

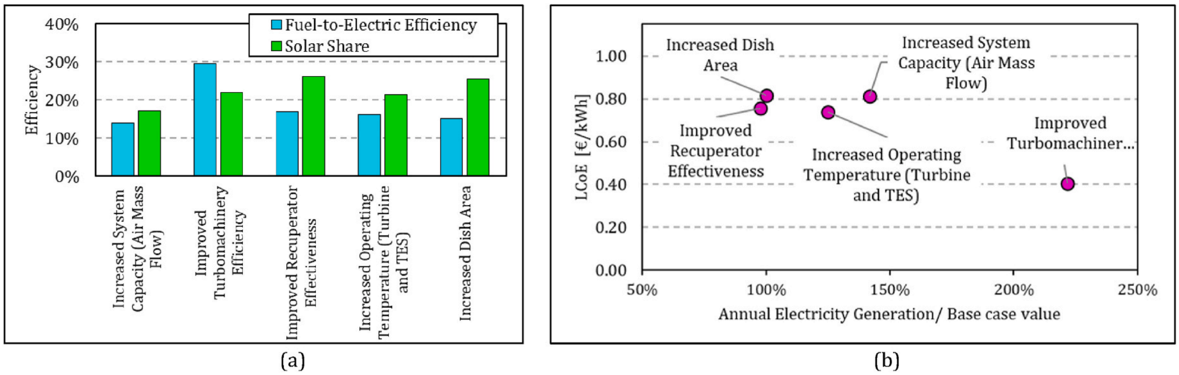

Fig. 21. Techno-economic impact of improving different aspects of the Solar-MGT system, with all scenarios adjusted to reflect similar CAPEX increases: (a) annual fuel-to-electric efficiency and solar share; (b) LCoE versus relative annual electricity generation.

3.7. Applicability, and limitations

The proposed framework is intended for dish-scale solar-assisted micro gas turbine systems in which solar thermal input, storage behaviour, and gas-turbine off-design performance interact under time-varying ambient and irradiance boundary conditions. Its main practical use is early-stage design-space evaluation: quantifying annual performance and LCoE sensitivities to key turbine-side and solar/TES-side parameters, and highlighting where diminishing returns arise when solar input, storage state, and operating constraints are coupled over the year. Because the model resolves component off-design behaviour, receiver losses, and TES charge–discharge behaviour in a consistent annual simulation loop, it is suitable for comparative assessment of alternative design configurations.

Extending the framework to substantially larger systems or different architectures (e.g., multi-dish fields, alternative storage layouts, or different control schemes, or similar cycles) is feasible but would require refinement of several sub-models.

In particular, scaling beyond the present dish-scale configuration would benefit from more detailed optical/receiver modelling (e.g., performance variation with incidence angle and potential field effects), explicit treatment of site- and technology-dependent degradation/ maintenance, and re-calibration of cost correlations to reflect manufacturing scale and balance-of-plant contributions. Larger concentrators exhibit size-dependent optical performance due to self-weight deformation, wind loading, tracking accuracy, mirror slope error and flux redistribution. Similarly, while the current component-map approach supports off-design evaluation, the quantified sensitivities may shift under alternative control strategies or actuator constraints, so design conclusions should be interpreted within the operating assumptions adopted in this work.

From a cost perspective, the LCoE values obtained for this system are significantly higher than current benchmarks for utility-scale PV, which are in the range of approximately 40–50 USD/MWh for newly commissioned plants. For context, over the 2010–2024 period the global weighted-average LCoE of utility-scale solar PV fell from 0.417 USD/ kWh in 2010 to 0.043 USD/kWh in 2024 [78]. The LCoE values reported here are instead consistent with the small scale of the system and with other small-scale solar-thermal concepts in the literature [79] and [38]. The present cost model also does not include mass-production or learning-curve effects: component costs are evaluated as if the system were manufactured in low volumes. Previous techno-economic studies on dish–micro gas turbine systems have shown that economies of scale can substantially reduce specific costs, by up to about 40% at high production rates [17]. Consequently, the LCoE figures presented in this work should be interpreted primarily as relative indicators for comparing trends and trade-offs between different design strategies within the proposed solar–MGT concept, rather than as fully optimised, market-ready benchmarks. A future, well-optimised system manufactured at high production volumes would be expected to achieve significantly lower LCoE, closer to those of more mature renewable technologies. The main value proposition of the solar–MGT–TES system, however, lies not in outperforming PV on pure LCoE, but in providing dispatchable electricity and high-temperature heat with integrated storage and fuel-based backup at decentralised scale, which is particularly relevant for remote, high-DNI sites and combined heat-and-power applications.

That said, the present results should be interpreted in the context of several modelling assumptions adopted to maintain tractability for annual parametric evaluation.

- The TES is represented as a lumped latent-heat storage whose state is tracked via stored internal energy and liquid fraction; therefore, spatial temperature gradients, phase-front dynamics, and detailed heat-transfer limitations within the PCM are not resolved. TES heat losses are treated using a simplified round-trip loss assumption, which captures the first-order impact of idle losses but does not represent insulation design or temperature-dependent loss mechanisms explicitly.
- The model is constructed in a quasi-steady manner at each time step; therefore, it does not resolve transients associated with shaft inertial dynamics, detailed component thermal inertia and heat-transfer dynamics, or solar-field tracking and control dynamics. These effects may be important for start-up/shut-down behaviour and short-timescale operation and should be addressed in future fully dynamic simulations.
- The solar receiver model uses a fixed optical/sky representation and does not include site-specific optical degradation, soiling, or detailed field effects such as shading; these factors could influence annual solar utilisation and should be examined in future refinements. The techno-economic evaluation relies on cost correlations and fixed financial assumptions, and the PCM-specific cost is derived via interpolation/regression from available literature data; these assumptions introduce uncertainty in absolute LCoE values, although the comparative trends across design variations remain valid and informative.

4. Conclusion

This work presented a detailed techno-economic investigation of a solar-assisted micro gas turbine system, supported by an experimentally validated off-design model and a full-year simulation using real meteorological data. Validation against controlled laboratory measurements and solar-assisted operation showed good agreement in receiver outlet temperatures and fuel flow rates, confirming the model's capability to capture both turbine behaviour and solar-thermal integration under varying operating conditions.

The main contributions of this study are.

- An experimentally validated, component-resolved off-design Solar-MGT performance model integrated with receiver and TES operation.
- A full-year simulation framework that propagates ambient/irradiance variability through turbine, receiver, and TES charge–discharge.
- An updated component-wise cost model and integrated techno-economic assessment that quantifies annual performance–cost sensitivities and reveals distinct cost–performance trajectories for turbine-side versus solar/TES-side design changes.

The parametric analysis revealed clear and quantifiable trade-offs between performance, flexibility, and cost. Turbine inlet temperature remains the dominant driver of system efficiency, but its economic benefit is constrained by diminishing LCoE reductions once recuperator and structural limits are approached. Dish area strongly increases solar fraction but exhibits nonlinear cost scaling, indicating an optimal range where gains in solar contribution balance increases in capital cost. Thermal energy storage improves dispatchability and reduces fuel use, though its marginal economic benefit depends on both mass and charging temperature; excessive storage capacity or very high melting temperatures do not yield proportional improvements in annual performance. Recuperator effectiveness enhances fuel efficiency but imposes a penalty through increased pressure losses and component cost, underscoring the need for balanced sizing rather than maximisation of any single parameter.

Overall, the results demonstrate that the most favourable techno-economic configurations emerge not from extreme parameter values but from combinations that balance solar input, thermal recuperation, and manageable TES operation. These findings have broader relevance for decentralised and off-grid applications, where reliable solar power provision must be achieved within tight cost constraints and variable environmental conditions. The identified performance–cost trade-offs and parameter sensitivities provide a structured basis for future multi-objective thermo-economic optimisation studies.

Future work should extend this framework to improved TES designs, alternative system configurations, and operational strategies that enhance part-load behaviour. Integrating power electronics, control architectures, and battery storage would enable a more realistic representation of field deployment. The modelling approach developed here is also transferrable to other high-temperature and hybrid energy systems, including closed-cycle CO_2 Brayton cycles, solar-assisted hydrogen generation, and multi-source renewable microgrids where similar parametric thermo-economic trade-offs between heat input, recuperation, and storage must be considered. Finally, applying the methodology across diverse geographic locations would clarify how regional solar availability and ambient conditions influence techno-economic performance and help identify the most favourable settings for Solar-MGT deployment.

CRediT authorship contribution statement

Vahid Hosseini: Writing – original draft, Visualization, Validation, Methodology, Investigation, Formal analysis. **Noura Bettaieb:** Writing – review & editing, Supervision, Project administration, Methodology. **Tehmina Ambreen:** Writing – review & editing, Supervision, Resources, Methodology, Funding acquisition.

Declaration of competing interest

The authors declare that they have no known competing financial interests or personal relationships that could have appeared to influence the work reported in this paper.

Data availability

Data will be made available on request.

References

[1] bp. Statistical review of world energy. 2022.
[2] Ding Z, Hou H, Duan L, Hu E, Zhang N, Song J. Performance analysis and capacity optimization of a solar aided coal-fired combined heat and power system. Energy 2022;239:122141. https://doi.org/10.1016/j.energy.2021.122141.
[3] Ya-Ling He and others. Perspective of concentrating solar power. Energy 2020;198:117373. https://doi.org/10.1016/j.energy.2020.117373.
[4] M. Boujoudar and others. AI fault detection in CSP with simulation based fault injection on a 1 MWe Fresnel–ORC plant. Sol Energy 2026;303(October 2025):114089. https://doi.org/10.1016/J.SOLENER.2025.114089.
[5] Pepermans G, Driesen J, Haeseldonckx D, Belmans R, D'haeseleer W. Distributed generation: definition, benefits and issues. Energy Policy 2005;33(6):787–98. https://doi.org/10.1016/J.ENPOL.2003.10.004.
[6] Hansen CJ, Bower J. An economic evaluation of small-scale distributed electricity generation technologies. 2003.
[7] Gonzalo AP, Marugán AP, Márquez FPG. A review of the application performances of concentrated solar power systems. Appl Energy 2019;255:113893. https://doi.org/10.1016/j.apenergy.2019.113893.
[8] Kasaeian A, Tabasi S, Ghaderian J, Yousefi H. A review on parabolic trough/Fresnel based photovoltaic thermal systems. Renew Sustain Energy Rev 2018;91:193–204. https://doi.org/10.1016/J.RSER.2018.03.114.
[9] Zayed ME, Zhao J, Elsheikh AH, Li W, Sadek S, Aboelmaaref MM. A comprehensive review on Dish/Stirling concentrated solar power systems: design, optical and geometrical analyses, thermal performance assessment, and applications. J Clean Prod Feb. 2021;283:124664. https://doi.org/10.1016/J.JCLEPRO.2020.124664.
[10] Malik MZ, et al. A review on design parameters and specifications of parabolic solar dish Stirling systems and their applications. Energy Rep Nov. 2022;8:4128–54. https://doi.org/10.1016/J.EGYR.2022.03.031.
[11] Bonasio V, Ravelli S. Performance analysis of an ammonia-fueled Micro gas turbine. 2022. https://doi.org/10.3390/en15113874.
[12] M. Jeremiah, B. Kabeyi, and O. A. Olanrewaju, "Decentralized and distributed power generation.".
[13] Gauché P, Brent AC, von Backström TW. Concentrating solar power: improving electricity cost and security of supply, and other economic benefits. Dev South Afr 2014;31(5):692–710. https://doi.org/10.1080/0376835X.2014.930791.
[14] Kasaeian A, Bellos E, Shamaeizadeh A, Tzivanidis C. Solar-driven polygeneration systems: recent progress and outlook. Appl Energy 2020;264:114764. https://doi.org/10.1016/j.apenergy.2020.114764.
[15] Alzaili J, Sayma AI. Challenges in the development of Micro gas turbines for concentrated solar power systems. In: The future of gas turbine technology. 8th International Gas Turbine Conference; 2016. p. 6.
[16] H.V. Kava and others. Decentralized DC solar power system for remote areas. Mater Today Proc 2023;73:590–4. https://doi.org/10.1016/J.MATPR.2022.11.279.
[17] Gavagnin G, Sánchez D, Martínez GS, Rodríguez JM, Muñoz A. Cost analysis of solar thermal power generators based on parabolic dish and micro gas turbine: manufacturing, transportation and installation. Appl Energy 2017;194:108–22. https://doi.org/10.1016/J.APENERGY.2017.02.052.
[18] Abdelhady S. Performance and cost evaluation of solar dish power plant: sensitivity analysis of levelized cost of electricity (LCOE) and net present value (NPV). Renew Energy 2021;168:332–42. https://doi.org/10.1016/J.RENENE.2020.12.074.
[19] Kesseli JB, Wells A. Cost competitive 30 kW gas turbine/generator demonstration for cogeneration or solar-electric applications. In: Proceedings of the 24th intersociety energy conversion engineering conference; 1989. p. 1903–8. https://doi.org/10.1109/IECEC.1989.74731.
[20] Banihabib R, Fadnes FS, Assadi M. Techno-economic optimization of microgrid operation with integration of renewable energy, hydrogen storage, and micro gas turbine. Renew Energy 2024;237:121708. https://doi.org/10.1016/J.RENENE.2024.121708.
[21] M. Lanchi and others. Investigation into the coupling of Micro gas turbines with CSP technology: OMSoP Project. Energy Proc 2015;69:1317–26. https://doi.org/10.1016/j.egypro.2015.03.146.
[22] P. O. of the E. Union. SOLGATE, solar hybrid gas turbine electric power system. 2005.
[23] C. E. U. research results (European Commission). SOLHYCO solar-hybrid power and cogeneration plants. 2011.
[24] R. Korzynietz and others. Solugas – comprehensive analysis of the solar hybrid Brayton plant. Sol Energy 2016;135:578–89. https://doi.org/10.1016/j.solener.2016.06.020.
[25] Ssebabi B, Dinter F, van der Spuy J, Schatz M. Predicting the performance of a micro gas turbine under solar-hybrid operation. Energy 2019;177:121–35. https://doi.org/10.1016/j.energy.2019.04.064.
[26] CORDIS EU research results (European Commission). Final Report Summary - OMSoP optimised microturbine solar power system. Publications Office; 2017 [Online]. Available: https://cordis.europa.eu/project/id/308952/reporting.
[27] C. Benhida, "D9.4 Final report on the project exploitation initiatives and related impacts on innovation, including Dissemination & Communication activities", doi: 10.5281/ZENODO.7299865..

[28] Le Roux WG, Sciacovelli A. Recuperated solar-dish Brayton cycle using turbocharger and short-term thermal storage. Sol Energy 2019;194:569–80. https://doi.org/10.1016/J.SOLENER.2019.10.081.
[29] Loni R, Asli-Ardeh EA, Ghobadian B, Bellos E, Le Roux WG. Numerical comparison of a solar dish concentrator with different cavity receivers and working fluids. J Clean Prod 2018;198:1013–30. https://doi.org/10.1016/J.JCLEPRO.2018.07.075.
[30] Jilte RD, Kedare SB, Nayak JK. Natural convection and radiation heat loss from open cavities of different shapes and sizes used with dish concentrator. Mech Eng Res 2013;3(1):25. https://doi.org/10.5539/MER.V3N1P25.
[31] Müller-Steinhagen H, Trieb F. Concentrating solar power; A review of technology. ingenia 2004;(18):43–50. https://doi.org/10.1016/B978-0-08-102886-5.00019-0.
[32] Le Roux WG, Meyer JP. Modeling the small-scale dish-mounted solar thermal Brayton cycle. AIP Conf Proc 2016;1734(1):60002. https://doi.org/10.1063/1.4949144.
[33] Le Roux WG, Bello-Ochende T, Meyer JP. Thermodynamic optimisation of the integrated design of a small-scale solar thermal Brayton cycle. Int J Energy Res 2012;36(11):1088–104. https://doi.org/10.1002/er.1859.
[34] Gallup D, Kesseli J. A solarized Brayton engine based on turbo-charger technology and DLR receiver. In: Intersociety energy conversion engineering conference, International Energy Conversion Engineering Conference (IECEC); 1994. https://doi.org/10.2514/6.1994-3945.
[35] Iaria D, Nipkey H, Al Zaili J, Sayma AI, Assadi M. Development and validation of a thermo-economic model for design optimisation and off-design performance evaluation of a pure solar microturbine. Energies 2018;11(11):3199. https://doi.org/10.3390/EN11113199.
[36] Lanchi M, Al-Zaili J, Russo V, Falchetta M, Montecchi M, Aichmayer L. A quasi-steady State model of a solar parabolic Dish Micro Gas turbine demonstration plant. Energies 2022;15:1059. https://doi.org/10.3390/en15031059.
[37] Hampel CA, Braun RJ. Off-design modeling of a microturbine combined heat & power system. Appl Therm Eng 2022;202:117670. https://doi.org/10.1016/j.applthermaleng.2021.117670.
[38] Ghavami M, Al-Zaili J, Sayma AI. A methodology for techno-economic and operation strategy optimisation of micro gas turbine-based solar powered dish-engine systems. Energy 2022;251:123873. https://doi.org/10.1016/j.energy.2022.123873.
[39] Giostri A, Macchi E. An advanced solution to boost sun-to-electricity efficiency of parabolic dish. Sol Energy 2016;139:337–54. https://doi.org/10.1016/J.SOLENER.2016.10.001.
[40] Semprini S, Sánchez D, De Pascale A. Performance analysis of a micro gas turbine and solar dish integrated system under different solar-only and hybrid operating conditions. Sol Energy 2016;132:279–93. https://doi.org/10.1016/J.SOLENER.2016.03.012.
[41] Rodríguez-deArriba P, Crespi F, Sánchez D. Towards cost-effective concentrating solar power: Techno-economic insights on transcritical CO2-based power cycles. Appl Therm Eng 2025;280:128369. https://doi.org/10.1016/J.APPLTHERMALENG.2025.128369.
[42] Fadzlin WA, Hasanuzzaman M, Rahman SA, Said Z. Solar thermal energy storage: global challenges, innovations, and future directions for renewable energy systems. Appl Therm Eng 2025;280:128346. https://doi.org/10.1016/J.APPLTHERMALENG.2025.128346.
[43] Nieto F, de la Calle A, Arias I, Cardemil JM, Bayon A, Escobar R. Annual performance of a calcium looping thermochemical energy storage with sCO2 Brayton cycle in a solar power tower. Energy 2025;336:138344. https://doi.org/10.1016/J.ENERGY.2025.138344.
[44] X. Chen and others. Techno-economic performance of the solar tower power plants integrating with 650 °C high-temperature molten salt thermal energy storage. Energy 2025;324:136073. https://doi.org/10.1016/J.ENERGY.2025.136073.
[45] Le Roux D, Olivès R, Neveu P. Multi-objective optimisation of a thermocline thermal energy storage integrated in a concentrated solar power plant. Energy 2024;300:131548. https://doi.org/10.1016/J.ENERGY.2024.131548.
[46] Yang Z, V Garimella S. Cyclic operation of molten-salt thermal energy storage in thermoclines for solar power plants. Appl Energy 2013;103:256–65. https://doi.org/10.1016/J.APENERGY.2012.09.043.
[47] Jian Y, Falcoz Q, Neveu P, Bai F, Wang Y, Wang Z. Design and optimization of solid thermal energy storage modules for solar thermal power plant applications. Appl Energy 2015;139:30–42. https://doi.org/10.1016/J.APENERGY.2014.11.019.
[48] Andraka CE, Kruizenga AM, Hernandez-Sanchez BA, Coker EN. Metallic phase change material thermal storage for dish Stirling. Energy Proc 2015;69:726–36. https://doi.org/10.1016/J.EGYPRO.2015.03.083.
[49] Humbert G, Roosendaal C, Swanepoel JK, Navarro HM, Le Roux WG, Sciacovelli A. Development of a latent heat thermal energy storage unit for the exhaust of a recuperated solar-dish Brayton cycle. Appl Therm Eng 2022;216:118994. https://doi.org/10.1016/J.APPLTHERMALENG.2022.118994.
[50] Behar O, Khellaf A, Mohammedi K. A review study for physical characteristics and engineering perspectives of dual molten salt tanks. Appl Therm Eng Jan. 2026;283:128840. https://doi.org/10.1016/j.rser.2013.02.017.
[51] Geissbühler L, Mathur A, Mularczyk A, Haselbacher A. An assessment of thermocline-control methods for packed-bed thermal-energy storage in CSP plants, part 1: method descriptions. Sol Energy Jan. 2019;178(2):341–50. https://doi.org/10.1016/j.solener.2018.12.015.
[52] V Hosseini S, Chen Y, Madani SH, Chizari M. Annual performance evaluation of a hybrid concentrated solar–micro gas turbine based on off-design simulation. Heliyon 2024;10(10):e30717. https://doi.org/10.1016/J.HELIYON.2024.E30717.
[53] Lee S, Mee DJ, Guan Z, Gurgenci H. Optimum combination of diesel and concentrating solar in remote area power generation using supercritical CO2 turbines. Energy Convers Manag 2023;278:116714. https://doi.org/10.1016/j.enconman.2023.116714.
[54] Z. Ding and others. Simulation study on a novel solar aided combined heat and power system for heat-power decoupling. Energy 2021;220:119689. https://doi.org/10.1016/j.energy.2020.119689.
[55] Galanti L, Massardo AF. Micro gas turbine thermodynamic and economic analysis up to 500 kWe size. Appl Energy 2011;88(12):4795–802. https://doi.org/10.1016/J.APENERGY.2011.06.022.
[56] Massardo AF, Scialò M. Thermoeconomic analysis of gas turbine based cycles. J Eng Gas Turbines Power 2000;122(4):664–71. https://doi.org/10.1115/1.1287346.
[57] Agazzani A, Massardo AF. A tool for thermoeconomic analysis and optimization of gas, steam, and combined plants. J Eng Gas Turbines Power 1997;119(4):885–92. https://doi.org/10.1115/1.2817069.
[58] Traverso A, Massardo AF. Optimal design of compact recuperators for microturbine application. Appl Therm Eng 2005;25(14–15):2054–71. https://doi.org/10.1016/J.APPLTHERMALENG.2005.01.015.
[59] Weerakoon AHS, Assadi M. Techno economic analysis and performance based ranking of 3–200 kW fuel flexible micro gas turbines running on 100% hydrogen, hydrogen fuel blends, and natural gas. J Clean Prod 2024;477:143819. https://doi.org/10.1016/J.JCLEPRO.2024.143819.
[60] Najafi B, Shirazi A, Aminyavari M, Rinaldi F, Taylor RA. Exergetic, economic and environmental analyses and multi-objective optimization of an SOFC-gas turbine hybrid cycle coupled with an MSF desalination system. Desalination 2014;334(1):46–59. https://doi.org/10.1016/J.DESAL.2013.11.039.
[61] Shirazi A, Aminyavari M, Najafi B, Rinaldi F, Razaghi M. Thermal–economic–environmental analysis and multi-objective optimization of an internal-reforming solid oxide fuel cell–gas turbine hybrid system. Int J Hydrogen Energy 2012;37(24):19111–24. https://doi.org/10.1016/J.IJHYDENE.2012.09.143.
[62] Reyhani HA, Meratizaman M, Ebrahimi A, Pourali O, Amidpour M. Thermodynamic and economic optimization of SOFC-GT and its cogeneration opportunities using generated syngas from heavy fuel oil gasification. Energy 2016;107:141–64. https://doi.org/10.1016/J.ENERGY.2016.04.010.
[63] A. Abuhaiba and others. Power transmission and control in microturbines' electronics: a review. Energies 2023;16(9). https://doi.org/10.3390/EN16093901.
[64] Weerakoon AHS, Assadi M. Techno-economic analysis and energy management strategies for micro gas turbines: a state-of-the-art review. Energy Convers Manag X Oct. 2024;24:100750. https://doi.org/10.1016/J.ECMX.2024.100750.
[65] Alva G, Liu L, Huang X, Fang G. Thermal energy storage materials and systems for solar energy applications. 2016. https://doi.org/10.1016/j.rser.2016.10.021.
[66] Swanepoel JK, et al. Initial experimental testing of a hybrid solar-dish Brayton cycle for combined heat and power (ST-CHP). Appl Therm Eng Jul. 2024;249:123275. https://doi.org/10.1016/J.APPLTHERMALENG.2024.123275.
[67] Brooks MJ, et al. SAURAN: a new resource for solar radiometric data in Southern Africa. J Energy South Afr Mar. 2015;26(1):2–10. https://doi.org/10.17159/2413-3051/2015/v26i1a2208. SE-Articles.
[68] Walsh PP, Fletcher P. Gas turbine performance. second ed. 2004.
[69] The MathWorks Inc. MATLAB version: 9.13.0 (R2022b). Natick, Massachusetts, United States: The MathWorks Inc.; 2022.
[70] GasTurb GmbH. GasTurb 15: Design and Off-Design Performance of Gas Turbines. Aachen, Germany: GasTurb GmbH; 2026. p. 71–81 [Online]. Available: https://www.gasturb.com/.
[71] Al Zaili J, Sayma AI, Iaria D. Reducing levelised cost of energy and environmental impact of a hybrid microturbine-based concentrated solar power plant. In: Proceedings of Shanghai 2017 global power and propulsion forum; 2017.
[72] Weerakoon AHS, Assadi M. Trends and advances in micro gas turbine technology for sustainable energy solutions: a detailed review. Energy Convers Manag X 2023;20:100483. https://doi.org/10.1016/J.ECMX.2023.100483.
[73] The chemical engineering plant cost index ® - chemical engineering.".
[74] Gavagnin G, Rech S, Sánchez D, Lazzaretto A. Optimum design and performance of a solar dish microturbine using tailored component characteristics. Appl Energy 2018;231:660–76. https://doi.org/10.1016/J.APENERGY.2018.09.140.
[75] Gavagnin G. Techno-Economic Optimization of a solar thermal power generator based on parabolic dish and Micro Gas turbine. 2019.
[76] Yan J, Peng YD, Liu YX. Wind load and load-carrying optical performance of a large solar dish/stirling power system with 17.7 m diameter. Energy Nov. 2023;283:129207. https://doi.org/10.1016/J.ENERGY.2023.129207.
[77] Yan J, Peng YD, Liu YX. Optical performance evaluation of a large solar dish/Stirling power generation system under self-weight load based on optical-mechanical integration method. Energy Feb. 2023;264:126386. https://doi.org/10.1016/J.ENERGY.2022.126386.
[78] IRENA. Renewable Power Generation Costs in 2024. Abu Dhabi: International Renewable Energy Agency; 2025. p. 86–107 [Online]. Available: https://www.irena.org/Publications/2025/Jun/Renewable-Power-Generation-Costs-in-2024.
[79] Giostri A, Binotti M, Sterpos C, Lozza G. Small scale solar tower coupled with micro gas turbine. Renew Energy Mar. 2020;147:570–83. https://doi.org/10.1016/j.renene.2019.09.013.